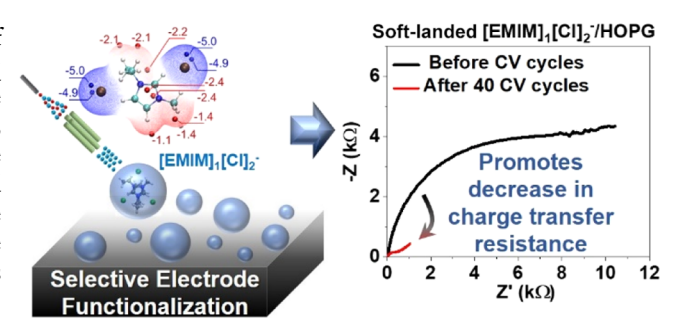
Functionalization of Electrodes with Tunable $[EMIM]_x[CI]_{x+1}$ lonic Liquid Clusters for Electrochemical Separations

Eric T. Baxter, Jun Zhang, Shuai Tan, Manh-Thuong Nguyen, Difan Zhang, Qinqin Yuan, Wenjin Cao, Xue-Bin Wang, Venkateshkumar Prabhakaran,* Vassiliki-Alexandra Glezakou,* and Grant E. Johnson*

ABSTRACT: Functionalization of electrodes with clusters of hydrophobic molecules may improve the energy efficiency and selectivity of electrochemical separations by modulating the desolvation process occurring at the interface. Ionic liquids (ILs), which have a broad range of compositions and properties, are potential candidates for controlling the transport, desolvation, and adsorption of target ions at electrochemical interfaces. Herein, we report a joint experimental and theoretical investigation of the structure, stability, and selective adsorption properties of IL clusters 1-ethyl-3-methylimidazolium chloride $[EMIM]_x[C1]_{x+1}^-$ (x=1-10) and demonstrate their ability to adsorb and separate



ions from solution. The structure and stability of the IL clusters are determined experimentally using high-mass-resolution electrospray ionization mass spectrometry, collision-induced dissociation, and negative-ion photoelectron spectroscopy. Global optimization theory and *ab initio* molecular dynamics simulations provide molecular-level insights into the bonding and structural fluxionality of these species. Ion soft landing is used to selectively functionalize the surface of highly oriented pyrolytic graphite (HOPG) working electrodes with $[EMIM]_1[Cl]_2^-$, $[EMIM]_3[Cl]_4^-$, and $[EMIM]_5[Cl]_6^-$ clusters. Kelvin probe microscopy provides insights into the relative stability of the clusters on HOPG and their effect on the work function of IL-functionalized electrodes. Cyclic voltammetry measurements reveal the irreversible adsorption of $Fe(CN)_6^{4-/3-}$ anions during redox cycling, while electrochemical impedance spectroscopy indicates a substantial decrease in the electron transfer resistance of the IL-functionalized electrodes due to adsorption of $Fe(CN)_6^{4-/3-}$. Overall, our findings demonstrate that IL clusters with different sizes and stoichiometry may be used to increase the efficiency of electrochemical separations, opening new horizons in selective electrode functionalization.

INTRODUCTION

Ionic liquids (ILs) are a subset of molten salts composed of organic cations and (in)organic anions with melting points commonly below T = 373 K. The distinguishing and often desirable properties of ILs, such as their low vapor pressure, high ionic conductivity, high thermal and chemical stability, and a wide stable electrochemical potential range, 1,2 have generated increasing attention to these chemicals for applications in energy storage,³⁻⁷ electrochemistry,⁸ cataly-sis,^{9,10} separations,^{11,12} designer/green solvents,¹³ and space propulsion technology.¹⁴ The physicochemical properties (e.g., melting point, surface tension, viscosity, and water miscibility) of ILs span a broad range and are dependent on the type of anion and/or cation constituting the liquid. 15 Due to the vast structural diversity of different ion pairs that form ILs, a unique opportunity exists to tune the physical and chemical properties of ILs for specific tasks. 16,17 However, rational design of taskspecific ILs requires a fundamental understanding of the interactions between cations and anions as well as how the structure of ILs evolves from the nano- and meso- to bulkscale. Indeed, the increasing number of models used to describe ILs suggests that they form complex structures at different length scales from supramolecular ^{18–23} (e.g., ion pairs and ion clusters) to mesoscopic ^{24–26} (e.g., H-bond networks, micelle-like phases, and bicontinuous morphologies).

Selective and efficient separation of target ions from solution is an important scientific challenge that is crucial to addressing global issues in energy production and consumption, environmental remediation, and energy efficiency in industry. ^{27–29} As the world population increases, separation processes will become an essential component to developing a sustainable future by providing clean water and extracting natural resources for energy storage and manufacturing. ^{30,31} Electro-

Received: November 6, 2021 Revised: February 12, 2022

chemical separation processes provide a sustainable platform for addressing water purification and wastewater treatment. Electrochemical approaches offer several advantages over traditional methods, such as fast kinetics, control through electric potential, reusability, and modularity.³²⁻³⁴ Furthermore, they generally require no additional chemicals during the regeneration stage and do not produce waste. It has been demonstrated that surface functionalization of electrodes may improve their selectivity and efficiency toward electrochemical adsorption of target ions and molecules. $^{35-37}$ For example, Wadhawan et al. observed the selective uptake of aqueous $Fe(CN)_6^{3-}$ into thin films of 1-methyl-3-(2,6-(S)-dimethylocten-2-yl)-imidazolium tetrafluoroborate deposited on a working electrode surface. 38 Desolvation of target ions at the electrochemical interface is one of the important energy-intensive processes that may be facilitated by the introduction of hydrophobic domains. 39,40 ILs with different chemical functionalities may offer a path for modulating the hydrophobicity and desolvation/adsorption processes of ions at electrode interfaces, thereby enabling energy-efficient and selective electrochemical separations. 36,41,42 However, understanding the molecular-level interactions between IL anions and cations that govern their larger scale structure, reactivity, and stability at interfaces is essential to developing new electrodes with tailored properties for ionic and molecular separations.

In this study, we investigate the formation and properties of anionic 1-ethyl-3-methylimidazolium chloride $[EMIM]_x[Cl]_{x+1}^-$ (x = 1-10) IL clusters and their suitability for enhancing the electrochemical adsorption and separation of ions from solution employing a combination of experiments and theory. First, we explore the size-dependent abundance and stability of anionic IL clusters in the gas phase where complicating factors present in the condensed phase, such as solvation, counter ions, and contaminants, are eliminated. The formation of IL clusters in solution is examined using highmass-resolution electrospray ionization mass spectrometry (ESI-MS), and their structures and relative stabilities toward dissociation are determined using collision-induced dissociation (CID) and the state-of-the-art global optimization theory. 43 Second, we obtain insights into the size- and composition-dependent electronic structure of IL clusters [i.e., electron binding energies (EBEs)] and benchmark our theoretical calculations using negative-ion photoelectron spectroscopy (NIPES). Third, we use electrostatic potential (ESP) maps calculated for the optimized structures of the $[EMIM]_x[C1]_{x+1}^-$ (x = 1-5) IL clusters to visualize favorable interaction sites for ion adsorption. Fourth, we use the insights obtained from the gas-phase experiments and calculations to prepare a set of IL-functionalized electrodes by soft-landing (SL) mass-selected $[EMIM]_x[Cl]_{x+1}^-$ (x = 1, 3, and 5) IL clusters onto the surface of highly oriented pyrolytic graphite (HOPG). We measure the work function of the soft-landed IL clusters on HOPG using spatially resolved amplitude modulation Kelvin probe force microscopy (AM-KPFM). Finally, we investigate the ion adsorption properties of the ILfunctionalized electrodes and demonstrate the applicability of size-selected IL clusters to tune the adsorption properties of electrodes for efficient separation of ions from solution using cyclic voltammetry (CV) and electrochemical impedance spectroscopy (EIS). Collectively, our results show that the size and structure of IL clusters play a dominant role in determining the energy barrier for ion desolvation/adsorption

and interfacial charge transfer, thereby providing a path for improving selective ion adsorption on functionalized electrodes during electrochemical separations.

EXPERIMENTAL METHODS

Mass Spectrometry. Mass spectra of the anionic IL clusters were

collected in the negative ion mode using a Thermo LTQ Orbitrap XL mass spectrometer equipped with an Ion Max atmospheric-pressure ionization (API) source operated in the ESI mode (Thermo Fisher Scientific, San Jose, CA). The mass spectrometer was operated over a mass range of $75-1600 \, m/z$ with the following settings: spray voltage, -3.5 kV; sheath gas flow, 20 units; capillary inlet temperature, T=150 °C; capillary voltage, -7 V; tube lens voltage, -70 V; and radiofrequency (RF) voltage peak-to-peak amplitude, 400 V. The instrument conditions were carefully optimized around the $[EMIM]_7[Cl]_8$ peak at m/z = 1061. We found that by tuning the instrument around a peak in the middle of the mass spectrum, the total abundances of the high-mass ions may be increased substantially with little effect on the relative abundances of the ions compared to one another. The voltage gradient between the capillary exit and tube lens was also adjusted to minimize in-source fragmentation of the ions. A sample [EMIM][Cl] solution was prepared with a concentration of 10 mM in methanol and introduced into the instrument through the API source using a syringe pump at a flow rate of 10 $\mu L/\text{min}$. CID measurements were performed by isolating individual charged clusters in the ion trap with an isolation window of $\Delta m/z = 10$ and using N₂ as an inert neutral collision partner to induce unimolecular dissociation. During CID, m/z isolated ions in the ion trap are kinetically excited with electric fields and collide with pure $N_2\,\text{gas}$ molecules leaked into the mass spectrometer. Multiple collisions convert the kinetic energy of the ions into internal vibrational excitation, which ultimately results in bond dissociation and formation of characteristic fragment ions. The relative stability of the parent cluster ions may be ascertained by analyzing the energy dependence of different ion fragmentation

Negative-Ion Photoelectron Spectroscopy. NIPES spectra of the anionic IL clusters were obtained using a magnetic-bottle time-offlight (TOF) photoelectron spectrometer combined with a homemade ÈSI source and a temperature-variable cryogenic ion trap. $[EMIM]_x[Cl]_{x+1}^-$ clusters were generated by spraying a ~ 0.1 mM methanolic solution of [EMIM][Cl] in the negative ion mode. The resulting anions were transported using an RF quadruple ion guide and first detected using a quadrupole mass spectrometer to optimize the ESI conditions to ensure stable and intense anion cluster beams. The anions were then directed using a 90° bender into the cryogenic 3D ion trap, where they were accumulated for 20-100 ms and cooled by collisions with a cold buffer gas (20% $\rm H_2$ balanced in He) to the desired temperature of 20 K before being pulsed out into the extraction zone of the TOF mass spectrometer for mass analysis at a repetition rate of 10 Hz. Each anion of interest was mass-selected and decelerated before being photodetached by a 157 nm (7.866 eV, Lambda Physik CompexPro F₂) laser beam in the interaction zone of the magnetic-bottle photoelectron analyzer. The probe laser was operated at a 20 Hz repetition rate with the anion beam shut off on alternating laser shots to afford shot-to-shot background subtraction. The resulting photoelectrons were collected at nearly 100% efficiency in the magnetic bottle and analyzed using a 5.2 m long electron flight tube. Recorded flight times were converted into calibrated kinetic energies. EBEs were obtained by subtracting the electron kinetic energies from the detachment photon energy with an energy resolution ($\Delta E/E$) of about 2% (i.e., ~20 meV for 1 eV kinetic energy electrons).

Ion Soft Landing. SL of anionic $[EMIM]_x[Cl]_{x+1}^{-}$ IL clusters was conducted by employing a custom-built high-flux ion deposition instrument that has been described in detail elsewhere. ^{47,48} Briefly, IL cluster anions were generated through ESI, introduced into vacuum using a high-transmission dual electrodynamic ion funnel interface, radially focused in a collision quadrupole, mass selected using a quadrupole mass filter, deflected 90° by a quadrupole bender, and

transferred to the surface through two einzel lenses in series. The HOPG substrates were mounted on a conductive stainless-steel bracket connected to a high-resistance electrometer (Keithley 6517A, Keithley Instruments, Cleveland, OH). The ion current was measured continuously throughout the deposition to accurately determine the total number of ions delivered to the surface. The ion current did not change substantially during the deposition. The kinetic energy of the ions impacting the surface was controlled by adjusting the potentials applied to the second collision quadrupole rods and the surface and was set to be $\sim\!20$ eV per charge for all of the experiments described herein. Based on atomic force microscopy measurements, the area of soft-landed material was around a few nanometers thick on the electrode surface.

Kelvin Probe Force Microscopy. The work functions of the IL/HOPG surfaces prepared by SL were characterized *via* AM-KPFM (NX10, Park Systems). Specifically, a tip coated with a chromium—platinum alloy (3 N/m spring constant, Budget Sensors) was used at a 75 kHz driving frequency and a peak-to-peak current amplitude that produced a tip cantilever displacement of 20 nm. One internal lock-in amplifier applied a 1 V AC bias with a 17 kHz frequency to distinguish the electrostatic force from the van der Waals force. By controlling the tip DC voltage through a feedback loop to keep the potential difference between the tip and the sample at zero, the value of the absolute surface potential and work function were calculated. Before measuring the IL samples, the tip was calibrated, and its work function was derived by using standard HOPG that has a work function of 4.65 eV.

Electrochemical Measurements. To investigate the ion adsorption and charge transfer properties of each SL $[EMIM]_x[Cl]_{x+1}^-$ cluster at the interface, electrochemical measurements were carried out *via* a three-electrode cell using $Fe(CN)_6^{3-/4-}$ as a redox probe molecule. Specifically, HOPG surfaces with selected SL clusters, referred to as $[EMIM]_x[Cl]_{x+1}$ -HOPG (x=1, 3, and 5), were used as the working electrodes. Pt wire and Ag/AgCl were used as the counter and reference electrodes, respectively. 0.1 M hydrochloric acid (HCl) with 0.05 M potassium ferricyanide (K₃[Fe(CN)₆]) was used as the electrolyte. A series of CV measurements were performed from -0.4 to 1 V at potential scan rates of 50, 20, 10, and 5 mV/s. 10 redox cycles $(Fe(CN)_6^{3-} \leftrightarrow Fe(CN)_6^{4-})$ were measured at each potential scan rate. The geometric area of the liquid contact region of the three-electrode cell is 0.478 cm², which is used to calculate the current density in the analysis of CV measurements. The change in the charge transfer resistance during ion adsorption was characterized using EIS, which was performed from 1 MHz to 1 Hz with a 5 mV amplitude before and after the series of CV measurements.

COMPUTATIONAL METHODS

Theoretical Calculations for [EMIM]x[Cl]x+1-. The structure of

each $[EMIM]_x[CI]_{x+1}^-$ (x = 1-7) IL cluster was searched using the artificial bee colony (ABC) global optimization algorithms 43,52-54 according to the following procedure: first, CHARMM force field parameters were designed for EMIM⁺ and Cl⁻ and the rigidmoloptimizer program of ABCluster^{52,53} was used to carry out the global optimization. The population size and number of generations were set to 100-2000 and 1000-2000, respectively, and the global optimization was performed up to 10 times with different starting structures. Then, 3000 structures for each species were optimized using NWPEsSe at the GFN2-xTB level of theory.⁵⁵ Finally, the 30 lowest energy structures were optimized at the B3PW91-D3/def2-SVP level of theory, 56-58 and the lowest energy structure was assigned as the global minima (GMs). Frequency analyses were then carried out to confirm that the structures are minima. Single-point energies were calculated for these minima using the domain-based local pair natural [DLPNO-CCSD(T)].59 coupled cluster $[EMIM]_x[Cl]_{x+1}^- x = 1-7$, the cc-pVTZ basis set was used, and for x = 1-3, a larger basis set (cc-pVQZ) was also used. The electron vertical detachment energies (VDEs) were calculated as the energy difference between the neutral unit and anion, both at the optimized

anion geometry. The electron adiabatic detachment energies (ADEs) were calculated as the energy difference between the neutral unit and anion at each optimized geometry including zero-point vibration energy correction. Both VDEs and ADEs were calculated at the DLPNO-CCSD(T)/cc-pVDZ level of theory. Ab initio molecular dynamics (AIMD) simulations, at the B3PW91-D3/def2-SVP level of theory, were performed for anionic $[EMIM]_2[CI]_3^-$ and neutral $[EMIM]_2[CI]_3^-$. The time step was 0.5 fs, and the temperature was controlled at 300 K using a Berendsen thermostat. The simulation time was 2.5 ps. The ESP maps of $[EMIM]_x[CI]_{x+1}^-$ (x = 1-5) were also calculated using the GM structures identified above at the B3PW91-D3/def2-SVP level of theory via Multiwfn. All ab initio calculations were carried out using ORCA 4.2.1.

RESULTS AND DISCUSSION

The formation of anionic $[EMIM]_x[CI]_{x+1}^-$ IL clusters in methanol solution at a concentration of 10 mM was investigated experimentally using high-mass-resolution $(m/\Delta m=60,000)$ ESI-MS. As shown in Figure 1, the negative-ion mode ESI mass spectrum reveals a broad distribution of anionic IL clusters with widely differing abundance. Specifi-cally, a series of peaks separated by a unit of $[EMIM][CI](\Delta m/z=146)$ was observed in the mass spectrum, consistent with singly charged anionic IL clusters with the molecular formula $[EMIM]_x[CI]_{x+1}^-$ for x=1-10 (red labeled peaks in Figure 1). From the mass spectrum presented in Figure 1, it is apparent that as the size of the IL clusters grows, they become increasingly able to accommodate additional CI^- anions, resulting in the formation of doubly charged [EMI-

M]_y[Cl]_{y+2}²⁻ clusters with y = 12-21. The doubly charged anions are evidenced by the emergence of an additional series of peaks located between the peaks assigned to the singly charged IL clusters beginning at m/z > 900. The spacing between the individual peaks that comprise the overall isotopic envelopes of each doubly charged IL cluster is equal to half (0.5) the spacing between the peaks of the singly charged IL clusters (1.0). Therefore, some of the singly and doubly charged IL clusters are mass degenerate and overlap in their nominal m/z values for even values of y in $[EMIM]_y[Cl]_{y+2}^{2-}$. As shown in the focused region displayed in the inset of Figure 1, the high mass resolution of the spectrum, combined with the differences in the isotopic distributions between the singly and

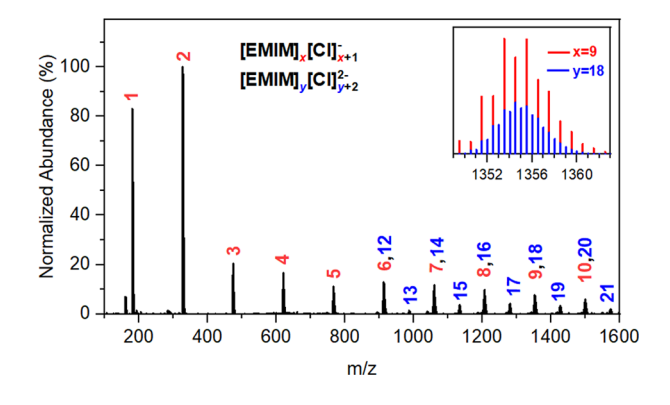


Figure 1. Representative mass spectrum of 10 mM [EMIM][CI] in methanol collected using ESI in the negative ion mode. The red and blue numbers designate singly and doubly charged anionic IL clusters with the stoichiometries $[EMIM]_x[CI]_{x+1}^-$ (red) and $[EMIM]_y[CI]_{y+2}^{2-}$ (blue), respectively. The *y*-axis is normalized to the most abundant anion (x = 2). The isotopic distributions of x = 9 (-1 charge, red) and y = 18 (-2 charge, blue) are shown in the inset.

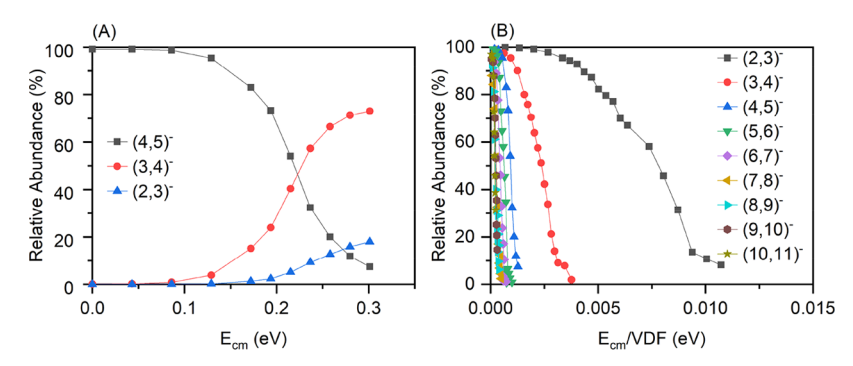


Figure 2. (A) Ion fragmentation yield curves for the representative mass-selected $[EMIM]_4[CI]_5^-$ IL cluster showing depletion of the precursor ion and formation of product fragment ions with increasing collision energy and (B) precursor ion survival curves for mass-selected $[EMIM]_x[CI]_{x+1}^-$ (x = 2-10) IL clusters. The x-axis has been converted to the center-of-mass collision energy (E_{cm}) and normalized to the number of vibrational degrees of freedom in each cluster. The (x,y) bracket notation indicates the number of EMIM⁺ cations and Cl⁻ anions in the cluster, respectively.

doubly charged IL clusters, allows us to unambiguously determine the contributions of both the 1- and 2-charge states to the overall total ion abundance. Experimental and theoretical investigation of the doubly charged 2-IL clusters is currently in progress and will be the focus of a forthcoming publication. Herein, we focus on the series of singly charged IL clusters. An interesting feature observed in the mass spectrum in Figure 1 is the pronounced variation in ion abundance with cluster size. This variation suggests that certain IL cluster structures may exhibit enhanced thermodynamic stability or are kinetically favored to be formed during the ESI process. 63-66 Similar trends in cluster ion abundance have been reported previously for imidazolium-based ILs. 67-70

Given the nonmonotonic trend in cluster abundance observed in Figure 1, the size-dependent stability of the IL clusters was investigated by measuring the fragmentation yield of mass-selected clusters as a function of their collision energy with nitrogen (N_2) molecules using CID experiments. The results of a representative CID measurement performed on mass-selected [EMIM]₄[Cl]₅ are presented in Figure 2A in the form of kinetic energy-dependent ion fragmentation yield curves. These curves were obtained by plotting the relative abundances of the mass-selected precursor ions and their associated fragment ions as a function of the collision energy with N_2 in the center-of-mass reference frame (E_{cm}) . At relatively low collision energies, the depletion of precursor ion [EMIM]₄[Cl]₅ is accompanied by the formation of [EMIM]₃[Cl]₄-, indicating that the major dissociation path-way is the loss of a neutral unit of [EMIM] [Cl], as shown in eq 1.

$$[EMIM]_4[Cl]_5^- \rightarrow [EMIM]_3[Cl]_4^- + [EMIM][Cl]$$
 (1)

As the collision energy is increased over 1.5 eV, fragment ion $[EMIM]_2[Cl]_3^-$ is also produced through sequential loss of two neutral [EMIM][Cl] units from $[EMIM]_4[Cl]_5^-$. Fragmentation *via* the loss of neutral [EMIM][Cl] units was observed as the major dissociation pathway for all of the singly charged $[EMIM]_x[Cl]_{x+1}^-$ clusters studied herein and is also comparable to the previously reported fragmentation behavior of $[EMIM]_n[BF_4]_{n+1}^-$ IL clusters.⁶⁹

Identical CID experiments were performed on all of the singly charged anionic IL clusters observed in Figure 1. To facilitate a qualitative comparison of relative cluster stability toward dissociation, precursor ion survival curves obtained from energy-dependent CID measurements of $[EMIM]_x[CI]_{x+1}^-(x=2-10)$ are presented in Figure 2B.

The survival curves represent the relative abundance of each mass-selected precursor ion as a function of the collision energy between the cluster ion and N2 normalized to the number of vibrational degrees of freedom of the IL clusters. This normalization accounts for variations in cluster stability resulting from a larger number of vibrational modes that may accommodate additional energy, consistent with the theory of unimolecular dissociation.⁷¹ The survival curves provide a qualitative understanding of the relative stabilities of the IL clusters as a function of size. Due to the limited low mass range of the mass spectrometer (50 < m/z), the fragmentation of the smallest [EMIM]₁[Cl]₂ IL cluster was not measured. The substantially higher dissociation energy of the [EMIM]₂[Cl]₃-IL cluster in Figure 2, in comparison to that of the larger clusters, highlights the enhanced stability of this species toward fragmentation, which is further corroborated by the large abundance of the [EMIM]₂[Cl]₃ cluster observed in the mass spectrum (Figure 1). The kinetic energies required to dissociate the IL clusters decrease by more than 50% as the cluster size increases from [EMIM]₂[Cl]₃⁻ to [EMIM]₃[Cl]₄⁻. For clusters with x > 3, the near overlap of the survival curves suggests that the stability of these IL clusters is similar.

To obtain experimental insights into the size-dependent electronic structure of the anionic IL clusters, we performed negative-ion photoelectron (NIPE) spectroscopy on $[\mathrm{EMIM}]_x[\mathrm{Cl}]_{x+1}^-$. The $T=20~\mathrm{K}$ NIPE spectra of $[\mathrm{EMIM}]_x[\mathrm{Cl}]_{x+1}^-$ (x=1-7) IL clusters, recorded at a photodetachment wavelength of 157 nm, are shown in Figure

3. The [EMIM]₁[Cl]₂⁻ cluster exhibits two energy-resolved peaks with maxima at EBEs of 5.20 and 5.53 eV, followed by a broad band at a higher EBE of approximately 7.2 eV. The ADE and VDE for [EMIM]₁[Cl]₂⁻ are measured from the onset threshold and peak maximum of the first band in the NIPE spectrum to be 5.02 and 5.20 eV, respectively (Table 1). In contrast, for IL clusters $[EMIM]_x[Cl]_{x+1}^-$ with x = 2-4, the NIPE spectra are composed of one band with a single maximum at low EBE, followed by a broad feature at higher EBE. Both the ADE and VDE show an ascending trend as the size of the IL clusters increases (Table 1), in a similar fashion to that of clusters of $[Na_xCl_{x+1}]^-$, $[Na_x(SCN)_{x+1}]^-$, and $[K_x(SCN)_{x+1}]^-$ that have been previously studied. ^{72,73} For the larger IL clusters (x = 5-7), each NIPE spectrum displays two bands. The main feature stems from the band seen in the spectra of the smaller clusters and shifts to higher EBE with increasing cluster size. The main bands at high EBE are assigned to singly charged $[EMIM]_x[C1]_{x+1}^-(x = 5-7)$

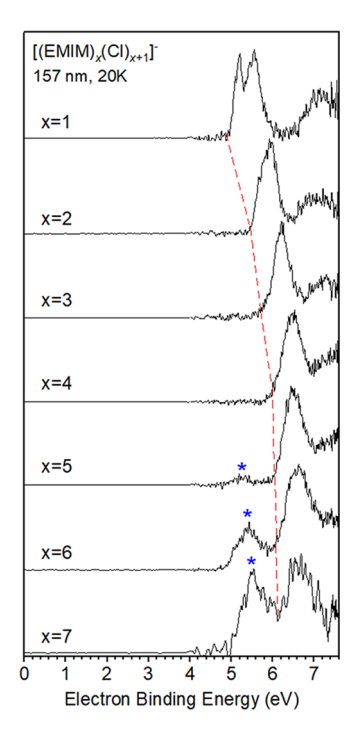


Figure 3. T = 20 K NIPE spectra of $[EMIM]_x[CI]_{x+1}^-$ (x = 1-7) IL clusters obtained at a photodetachment wavelength of 157 nm. The dashed red line serves as a guide for the ADE trend. The lower EBE band labeled as blue * in x = 5-7 is due to photodetachment of dianions $[EMIM]_y[CI]_{y+2}^-$ (y = 10, 12, and 14) with degenerate m/z values to those of the corresponding singly charged species x = 5, 6, and 7.

Table 1. Experimental (expt.) and Calculated (calc.) ADEs and VDEs of the $[EMIM]_x[Cl]_{x+1}^-(x=1-7)$ IL Clusters^a

		ADE (eV)		VDE (eV)
$[EMIM]_x[Cl]_{x+1}^-$	expt.	calc.	expt.	calc.
1	5.02	4.28	5.20	4.46
2	5.50	4.84	5.68	5.03
3	5.75	5.44	6.20	5.63
4	5.93	5.24	6.45	6.16
5	6.03	6.14	6.50	6.15
6	6.05	6.87	6.60	6.57
7	6.10	5.93	6.60	6.49

"Calculated values are obtained at the DLPNO-CCSD(T)/cc-pVDZ level of theory.

clusters based on their continuous evolution in both the band position and spectral profile in comparison to that of the smaller clusters (x = 1-4). The ADEs/VDEs of the larger IL clusters (x = 5-7) also increase with cluster size, albeit in smaller incremental steps (Table 1). The extra band appearing at lower EBE in Figure 3 (marked "*") is assigned to the doubly charged IL clusters $[EMIM]_y[Cl]_{y+2}^{2-}(y = 10, 12, and 14)$ that possess degenerate m/z values to the respective singly charged clusters (x = 5, 6, and 7). The coexistence of both singly and doubly charged clusters with degenerate m/z values in mass-selected ion beam experiments has been observed in a previous study of $[M_x(SCN)_{x+1}]^{-}/[M_{2x}(SCN)_{2x+2}]^{2-}$ (M = Na and K) clusters. The reason why doubly charged clusters possess lower EBEs than that of the half-sized singly charged anions is that the presence of additional excess charges in the doubly charged clusters results in strong intramolecular

Coulombic repulsion, leading to lower EBEs than that of singly charged IL clusters. The peak assignments in Figure 3 are also validated by theoretical calculations based on the good agreement between the measured and calculated ADE/VDE values of each cluster (Table 1). The intensity of the band assigned to the doubly charged IL clusters increases with the size of the cluster and is not present in the NIPE spectra for smaller clusters with x = 1-4. The absence of doubly charged anionic species in the small cluster size regime is due to larger Coulombic repulsion between the two excess charges leading to either electron autodetachment or breaking of chemical bonds. Detailed investigation of the structures and energetics of these larger doubly charged IL clusters will be the focus of a forthcoming publication.

Quantum chemical calculations were performed to identify the structures and energies of the IL clusters. The calculations also provide insights into the factors that contribute to the experimentally observed trends. The structures of $[EMIM]_x[CI]_{x+1}^-$ (x = 1-7) were searched using the ABC global optimization algorithm with both ABCluster 52,53 and NWPEsSe^{43,54} to obtain a wider range of molecular configurations. The structure ensembles were further screened using GFN2-xTB and B3PW91-D3/def2-SVP methods (see the Computational Methods section for details). The putative GMs are regarded as stable structures of these clusters and are shown in Figure 4A. Interestingly, for $x \le 3$, the structures of $[EMIM]_x[Cl]_{x+1}^-$ are similar to those of $[EMIM]_x[BF_4]_{x+1}^-$ reported in our previous work.⁶⁹ For $x \ge 4$, in the series of $[EMIM]_x[Cl]_{x+1}^{-}$, any additional $[EMIM]^+$ units occupy the outer shell of an $[EMIM]_3$ core (Figure 4B). Such disordered and liquid-like structures are a result of the gradual increase in attractive electrostatic interactions and occur earlier in the $[\mathrm{EMIM}]_x[\mathrm{Cl}]_{x+1}^-$ series when compared with that in $[\mathrm{EMIM}]_x[\mathrm{BF}_4]_{x+1}^{-.69}$ This difference in structural evolution with increasing cluster size may be explained by the smaller size of the Cl⁻ anion in comparison to that of the BF₄⁻ anion, which leads to a larger electric field density of the former.

To quantify the stability of the IL clusters relative to their building units as well as the energy of adding a building unit to the cluster or removing a unit from the cluster, the binding energies of the anionic IL clusters were computed using eq 2

$$E_{\rm B}(x) = [E(x) - xE_{\rm EMIM} \rightarrow (x + 1)E_{\rm Cl}^{-}]/(2x + 1)$$
 (2)

In addition, the second finite difference of energy $[\Delta^2 E_{\rm calc}(x)]$, which represents the average energy of adding or subtracting a building unit from a cluster, was calculated using eq.3.

$$\Delta^2 E_{\text{cal}}(x) = E(x+1) + E(x-1) - 2E(x$$
 (3)

In general, a large $\Delta^2 E_{\rm calc}$ value is indicative of a more stable cluster. These calculated quantities are plotted in Figure 5. The binding energy per ion approaches the limit of -2.7 eV as the size of the cluster increases. The peak at x=2 for $\Delta^2 E_{\rm calc}$ indicates that $[{\rm EMIM}]_2[{\rm Cl}]_3^-$ is highly stable, which agrees with the experimental observations from the ESI-MS abundance (Figure 1) and CID energy measurements (Figure 2).

For the $[EMIM]_x[Cl]_{x+1}^-$ clusters, x = 1-3, we computed the size-dependent ADE/VDE values with high accuracy using a DLPNO-CCSD(T)/cc-pVQZ quantum chemical method.⁷⁴ This method overcomes cancellation errors and provides reliable energies, which further validate that the GM structures

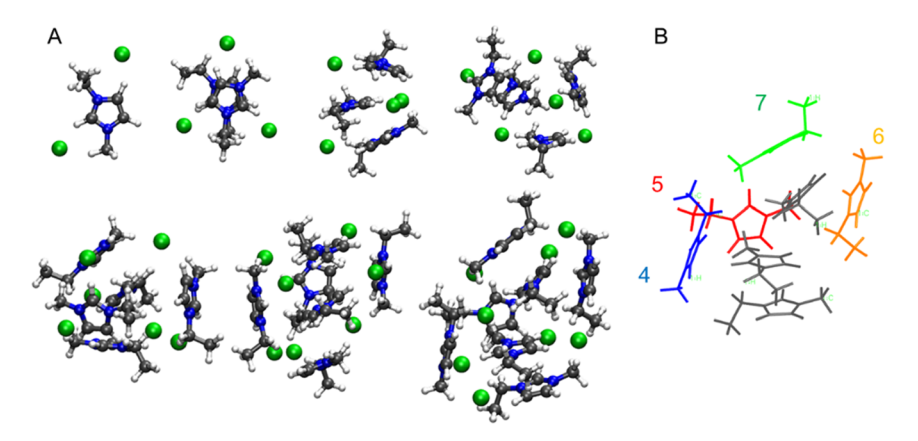


Figure 4. Calculated structures (A) and growth pattern (B) of $[EMIM]_x[Cl]_{x+1}^-$ (x = 1-7). The numbers in (B) indicate the sequence of additional $[EMIM]_x$ when x increases from 4 to 7.

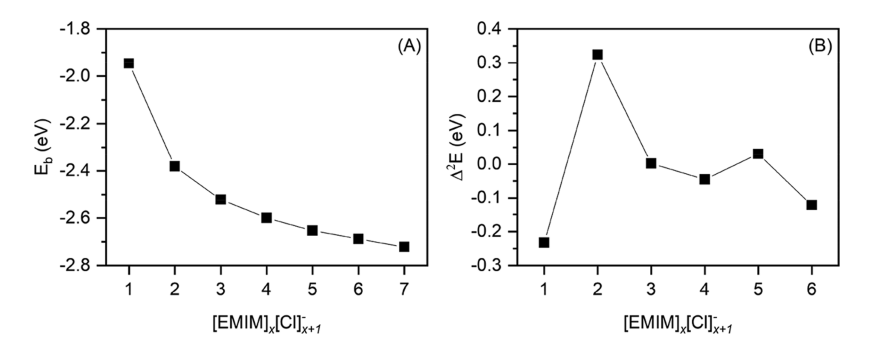


Figure 5. (A) Calculated binding energies for $[EMIM]_x[Cl]_{x+1}^-$ (x = 1-7). (B) Second difference of energy ($\Delta^2 E_{\text{calc}}$). Both energies were calculated at the DLPNO-CCSD(T)/cc-pVTZ level of theory.

(Table 2) are the dominant molecular configurations in the experiments. The VDEs were calculated as the energy difference between the neutral unit and anion, both at the optimized geometry of the anion. The ADEs were calculated as the energy difference between the neutral unit and anion at each optimized geometry including zero-point vibration energy correction. Here, the "optimized neutral geometry" was obtained by optimizing the neutral cluster starting from the

Table 2. Theoretically Predicted ADEs and VDEs of the $[\mathrm{EMIM}]_x[\mathrm{Cl}]_{x+1}^-(x=1-3)$ IL Clusters Compared with the Results of NIPES Experiments

	ADE (eV)		VDE	(eV)
$[EMIM]_x[Cl]_{x+1}^-$	expt.	calc. ^{a,b}	expt.	calc. ^a
1 (GM)	5.02	5.04	5.20	5.19
1 (LM: 0.50 eV)				4.46
2 (GM)	5.50	5.45	5.68	5.70
2 (LM: 0.19 eV)				6.27
3 (GM)	5.75	4.84 ^c	6.20	6.11
3 (LM: 0.07 eV)				5.89

^aEnergies were computed at the DLPNO-CCSD(T)/cc-pVQZ level ^{of} theory. The zero-point vibration energy corrections were computed at the B3PW91-D3/def2-SVP level of theory. ^cThe appreciably smaller calculated ADE relative to the experimental value is due to large geometrical changes for the corresponding neutral upon removal of one electron from the anion that results in negligible Franck—Condon overlap between the GM of the anion and the GM of the neutral unit; the experimental value in this case only represents an upper limit of the true ADE.

optimized geometry of the anion. The results are shown in Table 2.

The values calculated for the VDEs at GM geometries are in good agreement with the experimental NIPES values. For comparison, VDEs were also calculated at a local minimum (LM) geometry of each cluster, which yielded results quite different from the experimental values. For example, an LM of $[EMIM]_2[CI]_3^-$, which is energetically only 0.19 eV above the GM, exhibits a VDE value 0.59 eV higher than the experimental value. This provides evidence that in the gas phase, the most populated geometry of the IL cluster is the GM structure.

To explore the evolution of the IL clusters upon losing an electron, we performed two AIMD simulations starting from the GM of [EMIM]₂[Cl]₃-, but with different ionic charges (-1 and 0). These calculations were performed at the B3PW91D3/def2-SVP level of theory with the temperature held at T = 300 K. From the root-mean-square deviations (rmsds) of the atomic positions (Figure 6A), it is apparent that the structures of anionic [EMIM]₂[Cl]₃ and neutral [EMIM]₂[Cl]₃ become stable after 0.5 and 1.0 ps, respectively, with both about 1.25 eV energetically above the starting structures (Figure 6B). For anionic [EMIM]₂[Cl]₃⁻, the structure does not deviate substantially from its starting geometry throughout the whole simulation (Figure 7A), implying that the GM is relatively rigid on the potential energy surface. However, for neutral [EMIM]₂[Cl]₃, the electron density difference isosurface presented in Figure 7B suggests that upon detachment of an electron from the anionic cluster, the electron hole left behind is distributed over all of the three Cl⁻ anions, with minimal distribution over the two

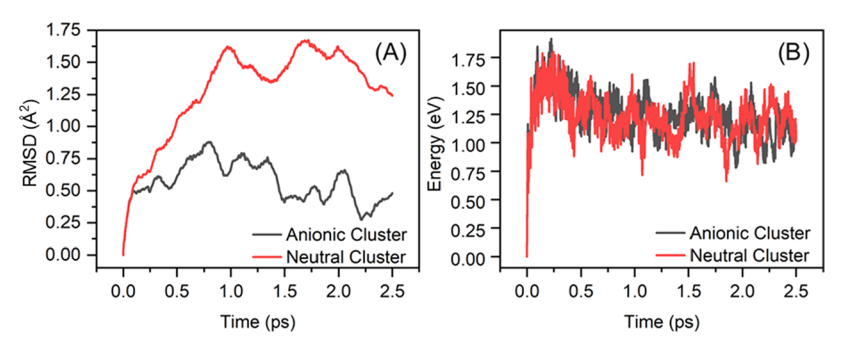


Figure 6. Results of AIMD simulations on anionic $[EMIM]_2[Cl]_3^-$ and neutral $[EMIM]_2[Cl]_3$: the RMSD (A) and potential energies (B) relative to those of the starting structures.

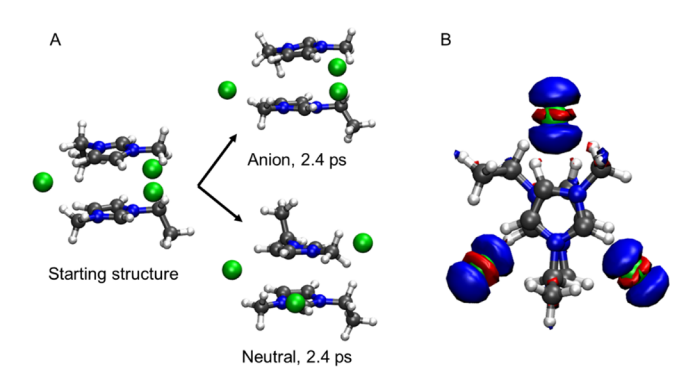


Figure 7. (A) Snapshots of AIMD simulations for $[EMIM]_2[Cl]_3^-$ at 2.4 ps. (B) Electron density difference between anionic $[EMIM]_2[Cl]_3^-$ and neutral $[EMIM]_2[Cl]_3$. The blue and red regions indicate where electron density decreases and increases after losing an electron, respectively. Isosurface value = 0.002 a.u.

EMIM⁺ cations. This charge distribution leads to weaker electrostatic interactions between ions and large fluctuations of the Cl⁻ positions (Figure 7A). Therefore, it may be inferred for $[\mathrm{EMIM}]_x[\mathrm{Cl}]_{x+1}^-$ that their GMs are the most populated structures in the gas phase. Upon detachment of one electron, all the Cl⁻ anions are directly affected and the charge of each chlorine ion is reduced by about -1/(x+1). The cluster relaxes to a nearby LM of the neutral cluster in several picoseconds.

The calculated ESP maps of the GM structures of the $[EMIM]_x[Cl]_{x+1}^-(x=1-5)$ clusters are compared in Figure 8. For the smallest cluster [EMIM][Cl]₂⁻, there are six ESP surface local maxima on the EMIM+ cation in the plane of the imidazole ring and two on either side of the ring. Two ESP surface LMs are identified on each Cl^- anion. The two Cl^- anions lie in the plane of the EMIM $^+$ cation to maximize their interaction with the cation and minimize mutual anion repulsion. For $[EMIM]_x[C1]_{x+1}^-$ (x = 2 and 3), the $EMIM^+$ cations are stacked perpendicular to the plane of the imidazole ring and the Cl⁻ anions reduce the electrostatic repulsion of the EMIM⁺ cations to stabilize the cluster. Additional EMIM⁺ cations and Cl⁻ anions in $[EMIM]_x[Cl]_{x+1}^-$ (x = 4 and 5) are also well-distributed to minimize electrostatic repulsion. A clear trend shows that both the magnitudes of the ESP maxima and minima become less negative from the smallest [EMIM]-[Cl]₂ cluster to the largest [EMIM]₅[Cl]₆⁻ cluster.

In a previous work, we demonstrated that functionalizing the surface of an HOPG working electrode with mass-selected $[\mathrm{EMIM}]_1[\mathrm{BF_4}]_2^-$ clusters resulted in a substantially lower charge transfer resistance in comparison to an HOPG

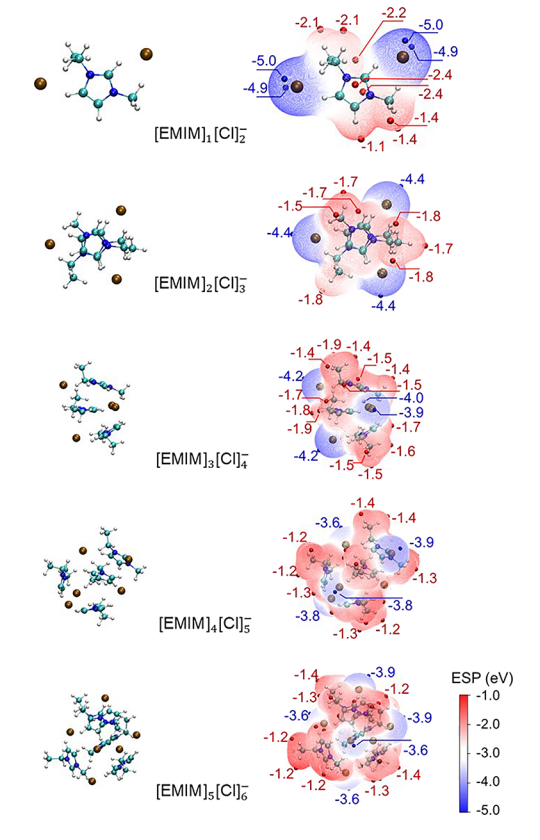


Figure 8. Calculated ESP maps of the van der Waals surface of $[\mathrm{EMIM}]_x[\mathrm{Cl}]_{x+1}^-$ (x=1-5). $\mathrm{ESP}_{\mathrm{max}}$ and $\mathrm{ESP}_{\mathrm{min}}$ are shown as red and blue regions, respectively.

electrode prepared using the traditional method of drop-casting a solution of $[EMIM][BF_4]$ that contains an undefined polydisperse mixture of ions. In this study, we investigate the effect of the size of [EMIM][Cl] clusters on the adsorption of ions by preparing working electrodes with different mass-selected $[EMIM]_x[Cl]_{x+1}$ (x=1,3, and 5) clusters using ion SL. The SL is a versatile and highly controlled method of preparing and modifying surfaces that avoids many of the complications inherent to conventional solution-based deposition methods. The SL is a versatile and highly controlled method of preparing and modifying surfaces that avoids many of the complications inherent to conventional solution-based deposition methods.

To determine the ion adsorption capacity of [EMIM][Cl] clusters SL on HOPG, a series of electrochemical measurements (CV and EIS) were performed using an aqueous solution containing the ferrocyanide–ferricyanide redox couple ${\rm Fe}({\rm CN})_6^{4-/3-}$ in 0.1 M HCl as the supporting electrolyte. The CV curves of the IL-functionalized HOPG electrodes were

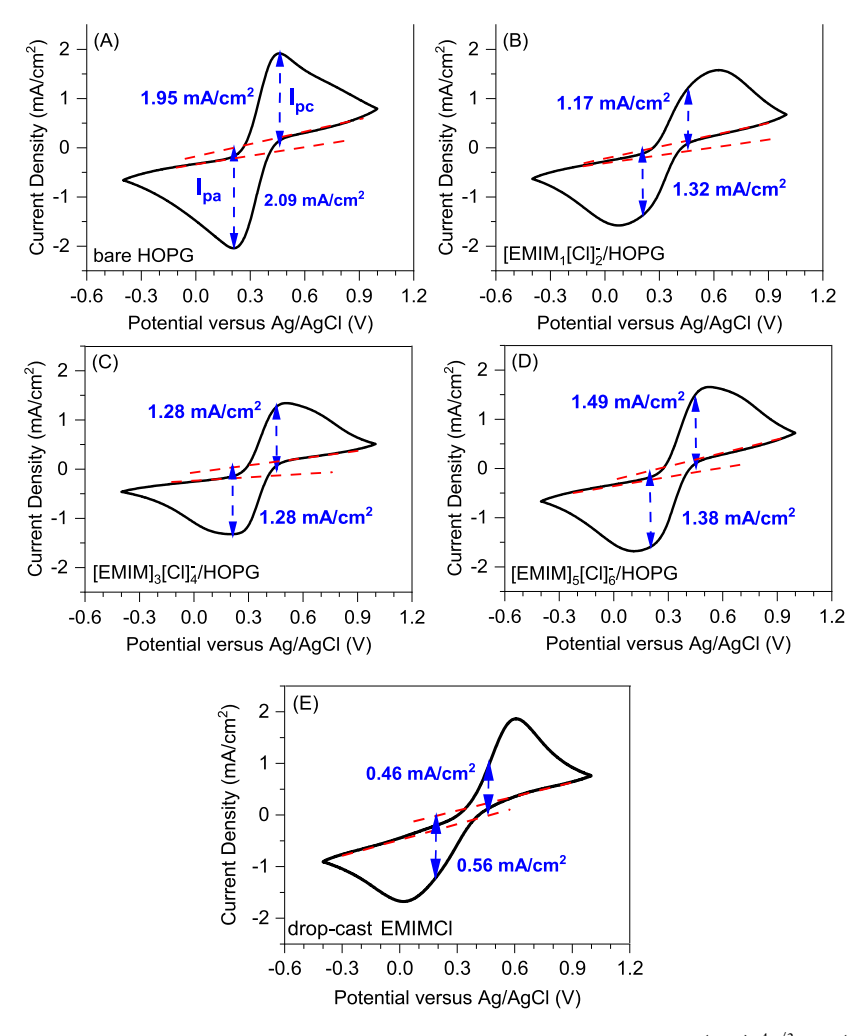


Figure 9. Representative CV curves obtained at a potential scan rate of 20 mV/s of the redox couple $Fe(CN)_6^{4-/3-}$ on (A) bare HOPG; IL-functionalized electrodes (B) $[EMIM]_1[CI]_2^-/HOPG$, (C) $[EMIM]_3[CI]_4^-/HOPG$, and (D) $[EMIM]_5[CI]_6^-/HOPG$ prepared by ion SL; and (E) drop-cast [EMIM][CI].

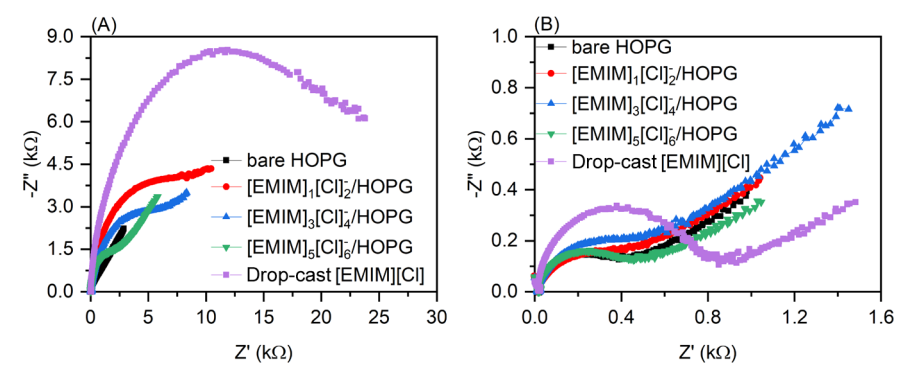


Figure 10. Nyquist plots of EIS measurements performed (A) before and (B) after 40 CV cycles on HOPG electrodes modified by drop-cast and SL $[EMIM]_x[Cl]_{x+1}^-$ (x = 1, 3, and 5) with an $Fe(CN)_6^{4-/3-}$ redox couple in 0.1 M KCl as the supporting electrolyte.

acquired at four different scan rates (50, 20, 10, and 5 mV/s) with 10 redox cycles at each scan rate (Figures 9 and S1). The potential difference between the anodic and cathodic peaks remained constant during all 40 CV cycles on the bare HOPG electrode, indicating fully reversible redox behavior of $Fe(CN)_6^{4-/3-}$. In contrast, the redox behavior of $Fe(CN)_6^{4-/3-}$ was partially irreversible on all four IL-function-alized electrodes, as revealed by the shift in peak potential as a function of scan rate. It should be noted that the full width at

half maximum (FWHM) of the redox peaks is greater than the theoretical value of 100 mV for a reversible one-electron transfer process. ⁸⁰ Compared to the CV curves on the bare HOPG electrode (Figure 9A) where only $Fe(CN)_6^{4-} \leftrightarrow Fe(CN)_6^{3-}$ takes place, the broader redox peaks shown for the HOPG electrodes with soft-landed EMIMCl clusters (Figure 9B–D) indicate multiple redox reactions, which may be due to the $Fe(CN)_6^{4-/3-}$ redox process occurring both (i) directly on HOPG and (ii) on EMIMCl clusters at the interface where

Table 3. Summary of the Quantity of SL Cluster Ions, Work Function, and Charge Transfer Resistance Values before and after CV Cycles Performed on Bare HOPG and $[EMIM]_x[Cl]_{x+1}^-/HOPG$ (x = 1, 3, and 5) Electrodes Prepared by Ion SL

electrode	total soft-landed ions	work function (eV)	charge transfer resistance before CV (Ω) charge transfer resistance after CV		
bare HOPG		4.65	700	407	
$[EMIM]_1[Cl]_2^-/HOPG$	6.6×10^{13}	4.06 ± 0.05	7289	620	
$[EMIM]_3[Cl]_4^-/HOPG$	5.5×10^{13}	4.36 ± 0.02	5425	604	
$[EMIM]_{5}[Cl]_{6}^{-}/HOPG$	8.0×10^{13}	4.49 ± 0.02	2232	617	
drop-cast [EMIM][Cl]	1.6×10^{14}	4.27 ± 0.03	23225	915	

additional electron transfer processes take place between the EMIMCl cluster and the underlying HOPG electrode. The limited peak resolution in the voltammograms introduces uncertainties into the process of deconvoluting the broad redox peaks into multiple components. Therefore, we used the peak potentials from the sharp redox peaks of $Fe(CN)_6^{4-/3-}$ on bare HOPG to estimate the relative concentrations of $Fe(CN)_6^{4-/3-}$ at the electrode interface of the IL-function-alized HOPG electrodes, as shown in Figure 9. The fitting process revealed a substantial decrease in the peak current densities of the ${\rm Fe}({\rm CN})_6^{4-/3-}$ redox components on the IL-functionalized electrodes, indicating that less ${\rm Fe}({\rm CN})_6^{4-/3-}$ participated in the redox process at the electrode interface in comparison to that on bare HOPG. The loss of $Fe(CN)_6^{4-/3-}$ may be attributed to formation of electrochemically inactive Fe(CN)₆-IL complexes during the redox process. Addition-ally, the decrease in the reversibility of the IL-functionalized electrodes compared to that on bare HOPG may be attributed to a lower electron transfer rate through the [EMIM][Cl] layers on HOPG. Therefore, EIS measurements were performed to assesses the changes in the charge transfer behavior of IL-functionalized HOPG before and after adsorption of $Fe(CN)_6^{4-/3-}$ during the redox cycles.

The initial EIS measurements, obtained prior to 40 CV cycles, revealed a high charge transfer resistance for the drop-cast and all three SL IL-functionalized electrodes in comparison to that of bare HOPG (Figure 10A). As expected, the initial charge transfer resistance of the drop-cast [EMIM]-[Cl] electrode is substantially higher than that of the SL and bare HOPG electrodes. The high charge transfer resistance may be attributed to the presence of larger IL clusters or formation of aggregates on the drop-cast electrode that may impede charge transfer at the interface (Figure 1). However, for the SL $[EMIM]_x[Cl]_{x+1}^-$ (x = 1, 3, and 5) clusters, the initial charge transfer resistance decreased as the size of the deposited IL cluster increased, a trend that is opposite to what is expected considering that the total number of ions deposited on each surface (Table 3) was the same order of magnitude.

These results suggest that the smaller SL clusters may aggregate on the surface to form larger clusters or the larger clusters may dissociate upon collision with the surface, resulting in deposition of smaller fragments. Both possibilities may affect the surface ionic conductivity of IL-functionalized electrodes due to changes in the size and charge density of the supported IL clusters.

EIS measurements obtained following 40 CV cycles revealed a substantial decrease in the charge transfer resistance of all four IL-functionalized electrodes (Figure 10B). No change was observed in the EIS spectrum of bare HOPG after cycling. The substantial decrease in electron transfer resistance after cycling suggests that the irreversible adsorption of ${\rm Fe(CN)_6}^{4-/3-}$ on the [EMIM][Cl] layers during the redox cycles results in an increase in the electron transfer rate through the layers. 82,83

The electrode functionalized with SL [EMIM]₁[Cl]₂⁻ clusters showed the largest anion adsorption capacity, as evidenced by the largest percent decrease in electron transfer resistance after cycling. It should be noted that by comparing to the initial electron transfer resistance before CV cycling, the drop-cast EMIMCl showed a 95% decrease after 40 CV cycles, whereas [EMIM]₁[Cl]₂ showed a 92% decrease. We speculate that the reason for the larger decrease in electron transfer resistance for the drop-cast electrode may be due to the presence of a higher number of mixed EMIMCl ions, which is almost 3 times higher than that for SL [EMIM]₁[Cl]₂-. The higher number of EMIMCl ions on the drop-cast electrode may eventually adsorb more $Fe(CN)_6^{4-/3-}$ and show a larger decrease in the electron transfer resistance than that of the SL electrodes. However, it should be noted that if we consider normalizing the decrease in electron transfer resistance to the number of ions at the electrode, the SL electrodes still demonstrate the largest decrease in electron transfer resistance.

To obtain further insights into the relative changes in the electronic properties of the SL clusters on HOPG, Kelvin probe microscopy was used to measure the work function at ambient conditions. The work function showed an ascending trend with increasing cluster size, in a similar fashion to the ADEs of the gas-phase IL clusters measured using NIPES (Figure 3). These results indicate an increase in electronic stability with increasing cluster size, which may be attributed to the formation of core—shell-like structures, as predicted by theory (Figure 4). Consequently, the work function and ADE values correlate with the decreasing trend in charge transfer resistance observed in the EIS measurements. These trends demonstrate that the initial size of the IL clusters SL on HOPG defines the electronic stability and adsorption capacity of Fe(CN)₆^{4-/3-} on the IL-functionalized electrodes.

CONCLUSIONS

Electrodes modified with specific chemical functionalities are promising active interfaces for the energy-efficient and selective electrochemical separation of target ions and molecules from water. ILs, which are molten salts with a wide variety of chemical and physical properties, are versatile materials that may be used to modulate the transport, desolvation, and adsorption of selected ions at complex electrochemical interfaces. Herein, we reported a combined experimental and theoretical examination of the geometric and electronic structure as well as the stability of $[EMIM]_x[Cl]_{x+1}^-(x=1-10)$ IL clusters and established their ability to efficiently adsorb and separate ions from aqueous solution when deposited on electrodes. The structural properties and stability of the IL clusters toward dissociation were investigated using high-massresolution ESI-MS, CID, and NIPES experiments in the gas phase. We obtained molecular-level insights into the bonding, structural rigidity, and electrostatic properties of the IL clusters using global optimization theory and ab initio MD

simulations. Representative $[EMIM]_1[Cl]_2^-$, $[EMIM]_3[Cl]_4^-$, and $[EMIM]_5[Cl]_6^-$ IL clusters were selectively deposited onto HOPG working electrodes using SL of mass-selected ions. The relative stability of the SL clusters on HOPG and the work function of the IL-functionalized electrodes were characterized using scanning Kelvin probe microscopy. CV measurements showed the partially irreversible redox behavior of $Fe(CN)_6^{4-/3-}$, while EIS indicated a substantial reduction in the electron transfer resistance of the working IL-functionalized electrode as a result of $Fe(CN)_6^{4-/3-}$ adsorption following redox cycling. Collectively, our findings demonstrate that size-selected IL clusters may be used to modulate the selective adsorption behavior and improve the efficiency of electrochemical separations at the functionalized interfaces.

ASSOCIATED CONTENT

Supporting Information

The Supporting Information is available free of charge at https://pubs.acs.org/doi/10.1021/acs.chemmater.1c03836.

Cyclic voltammograms measured on all IL/HOPG electrodes with an $Fe(CN)_6^{4-/3-}$ redox couple at different potential scan rates (5, 10, and 20 mV/s); equivalent circuit model used to fit the EIS data presented in Figure 10; and calculated frequencies for $[(EMIM)_x(Cl)_{x+1}]^-$ (PDF) Calculated structure of $[EMIM]_x[Cl]_{x+1}^-$ (x=1) (XYZ) Calculated structure of $[EMIM]_x[Cl]_{x+1}^-$ (x=2) (XYZ) Calculated structure of $[EMIM]_x[Cl]_{x+1}^-$ (x=3) (XYZ) Calculated structure of $[EMIM]_x[Cl]_{x+1}^-$ (x=4) (XYZ) Calculated structure of $[EMIM]_x[Cl]_{x+1}^-$ (x=5) (XYZ) Calculated structure of $[EMIM]_x[Cl]_{x+1}^-$ (x=6) (XYZ) Calculated structure of $[EMIM]_x[Cl]_{x+1}^-$ (x=6) (XYZ) Calculated structure of $[EMIM]_x[Cl]_{x+1}^-$ (x=6) (XYZ)

AUTHOR INFORMATION

Corresponding Authors

Venkateshkumar Prabhakaran — Physical and Computational Sciences Directorate, Pacific Northwest National Laboratory, Richland, Washington 99354, United States; orcid.org/0000-0001-6692-6488; Email: Venky@pnnl.gov

Vassiliki-Alexandra Glezakou — Physical and Computational Sciences Directorate, Pacific Northwest National Laboratory, Richland, Washington 99354, United States; orcid.org/ 0000-0001-6028-7021; Email: Vanda.Gleakou@pnnl.gov

Grant E. Johnson – Physical and Computational Sciences

Directorate, Pacific Northwest National Laboratory, Richland, Washington 99354, United States; orcid.org/ 0000-0003-3352-4444; Email: Grant.Johnson@pnnl.gov

Authors

Eric T. Baxter — Physical and Computational Sciences Directorate, Pacific Northwest National Laboratory, Richland, Washington 99354, United States

Jun Zhang — Physical and Computational Sciences Directorate, Pacific Northwest National Laboratory, Richland, Washington 99354, United States

Shuai Tan - Physical and Computational Sciences Directorate,

Pacific Northwest National Laboratory, Richland, Washington 99354, United States; orcid.org/0000-0001-8936-0106

Manh-Thuong Nguyen — Physical and Computational Sciences Directorate, Pacific Northwest National Laboratory, Richland, Washington 99354, United States

Difan Zhang — Physical and Computational Sciences Directorate, Pacific Northwest National Laboratory, Richland, Washington 99354, United States

Qinqin Yuan — Physical and Computational Sciences
Directorate, Pacific Northwest National Laboratory,
Richland, Washington 99354, United States Wenjin
Cao — Physical and Computational Sciences
Directorate, Pacific Northwest National Laboratory,
Richland, Washington 99354, United States; orcid.org/

Xue-Bin Wang — Physical and Computational Sciences
Directorate, Pacific Northwest National Laboratory,
Richland, Washington 99354, United States; orcid.org/
0000-0001-8326-1780

Complete contact information is available at: https://pubs.acs.org/10.1021/acs.chemmater.1c03836

Author Contributions

0000-0002-2852-4047

The manuscript was written through contributions of all authors. All authors have given approval to the final version of the manuscript.

Notes

The authors declare no competing financial interest.

ACKNOWLEDGMENTS

This work was supported by the U.S. Department of Energy (DOE), Office of Science, Office of Basic Energy Sciences, Chemical Sciences, Geosciences, and Biosciences Division, project 72353 (Interfacial Structure and Dynamics in Separations). The NIPES work was supported by the U.S. Department of Energy (DOE), Office of Science, Office of Basic Energy Sciences, Division of Chemical Sciences, Geosciences, and Biosciences (Chemical Kinetics and Dynamics at Interfaces). Part of this work was performed using EMSL, a National Scientific User Facility sponsored by the DOE's Office of Biological and Environmental Research and located at the Pacific Northwest National Laboratory (PNNL). The PNNL is a multiprogram national laboratory operated by Battelle for the U.S. Department of Energy under contract DE-AC05-76RL01830. Computer resources were provided by Research Computing at the PNNL and the National Energy Research Scientific Computing Center (NERSC), a DOE Office of Science User Facility operated under contract DE-AC02-05CH11231.

REFERENCES

- (1) Suarez, P. A. Z.; Selbach, V. M.; Dullius, J. E. L.; Einloft, S.; Piatnicki, C. M. S.; Azambuja, D. S.; de Souza, R. F.; Dupont, J. Enlarged electrochemical window in dialkyl-imidazolium cation based room-temperature air and water-stable molten salts. *Electrochim. Acta* 1997, 42, 2533–2535.
- (2) McEwen, A. B.; Ngo, H. L.; LeCompte, K.; Goldman, J. L. Electrochemical Properties of Imidazolium Salt Electrolytes for Electrochemical Capacitor Applications. *J. Electrochem. Soc.* **1999**, *146*, 1687–1695.
- (3) Liu, H.; Yu, H. Ionic liquids for electrochemical energy storage devices applications. *J. Mater. Sci. Technol.* **2019**, *35*, 674–686.
- (4) Kar, M.; Tutusaus, O.; MacFarlane, D. R.; Mohtadi, R. Novel and versatile room temperature ionic liquids for energy storage. *Energy Environ. Sci.* **2019**, *12*, 566–571.

- (5) MacFarlane, D. R.; Tachikawa, N.; Forsyth, M.; Pringle, J. M.; Howlett, P. C.; Elliott, G. D.; Davis, J. H.; Watanabe, M.; Simon, P.; Angell, C. A. Energy applications of ionic liquids. *Energy Environ. Sci.* **2014**, *7*, 232–250.
- (6) Fiore, M.; Wheeler, S.; Hurlbutt, K.; Capone, I.; Fawdon, J.; Ruffo, R.; Pasta, M. Paving the Way toward Highly Efficient, High-Energy Potassium-Ion Batteries with Ionic Liquid Electrolytes. *Chem. Mater.* **2020**, *32*, 7653–7661.
- (7) Lourenço, T. C.; Zhang, Y.; Costa, L. T.; Maginn, E. J. A molecular dynamics study of lithium-containing aprotic heterocyclic ionic liquid electrolytes. *J. Chem. Phys.* **2018**, *148*, 193834.
- (8) Armand, M.; Endres, F.; MacFarlane, D. R.; Ohno, H.; Scrosati, B. Ionic-liquid materials for the electrochemical challenges of the future. *Nat. Mater.* **2009**, *8*, 621–629.
- (9) Zhang, S.; Sun, J.; Zhang, X.; Xin, J.; Miao, Q.; Wang, J. Ionic liquid-based green processes for energy production. *Chem. Soc. Rev.* **2014**, *43*, 7838–7869.
- (10) Chen, Y.; Mu, T. Conversion of CO 2 to value-added products mediated by ionic liquids. *Green Chem.* **2019**, *21*, 2544–2574.
- (11) Sun, P.; Armstrong, D. W. Ionic liquids in analytical chemistry. *Anal. Chim. Acta* **2010**, *661*, 1–16.
- (12) Lee, J. S.; Luo, H.; Baker, G. A.; Dai, S. Cation Cross-Linked Ionic Liquids as Anion-Exchange Materials. *Chem. Mater.* **2009**, *21*, 4756–4758.
- (13) Erdmenger, T.; Guerrero-Sanchez, C.; Vitz, J.; Hoogenboom, R.; Schubert, U. S. Recent developments in the utilization of green solvents in polymer chemistry. *Chem. Soc. Rev.* **2010**, *39*, 3317–3333.
- (14) Roy, H. A.; Hamlow, L. A.; Rodgers, M. T. Gas-Phase Binding Energies and Dissociation Dynamics of 1-Alkyl-3-Methylimidazolium Tetrafluoroborate Ionic Liquid Clusters. *J. Phys. Chem. A* **2020**, *124*, 10181–10198.
- (15) Nacham, O.; Clark, K. D.; Yu, H.; Anderson, J. L. Synthetic Strategies for Tailoring the Physicochemical and Magnetic Properties of Hydrophobic Magnetic Ionic Liquids. *Chem. Mater.* **2015**, *27*, 923–931.
- (16) Wang, C.; Luo, X.; Luo, H.; Jiang, D.-e.; Li, H.; Dai, S. Tuning the Basicity of Ionic Liquids for Equimolar CO2 Capture. *Angew. Chem., Int. Ed.* **2011**, *50*, 4918–4922.
- (17) Thapaliya, B. P.; Puskar, N. G.; Slaymaker, S.; Feider, N. O.; Do-Thanh, C.-L.; Schott, J. A.; Jiang, D.-e.; Teague, C. M.; Mahurin, S. M.; Dai, S. Synthesis and Characterization of Macrocyclic Ionic Liquids for CO2 Separation. *Ind. Eng. Chem. Res.* **2021**, *60*, 8218–8226.
- (18) Izgorodina, E. I.; MacFarlane, D. R. Nature of Hydrogen Bonding in Charged Hydrogen-Bonded Complexes and Imidazolium-Based Ionic Liquids. *J. Phys. Chem. B* **2011**, *115*, 14659–14667.
- (19) Neto, B. A. D.; Meurer, E. C.; Galaverna, R.; Bythell, B. J.; Dupont, J.; Cooks, R. G.; Eberlin, M. N. Vapors from Ionic Liquids: Reconciling Simulations with Mass Spectrometric Data. *J. Phys. Chem. Lett.* **2012**, *3*, 3435–3441.
- (20) Wang, C.; Luo, H.; Li, H.; Dai, S. Direct UV-spectroscopic measurement of selected ionic-liquid vapors. *Phys. Chem. Chem. Phys.* **2010**, *12*, 7246–7250.
- (21) Triolo, A.; Russina, O.; Bleif, H.-J.; Di Cola, E. Nanoscale segregation in room temperature ionic liquids. *J. Phys. Chem. B* **2007**, *111*, 4641–4644.
- (22) Ludwig, R. Simple Geometrical Explanation for the Occurrence of Specific Large Aggregated Ions in Some Protic Ionic Liquids. *J. Phys. Chem. B* **2009**, *113*, 15419–15422.
- (23) Anthony, J. L.; Anderson, J. L.; Maginn, E. J.; Brennecke, J. F. Anion Effects on Gas Solubility in Ionic Liquids. *J. Phys. Chem. B* **2005**, 109, 6366–6374.
- (24) Greaves, T. L.; Drummond, C. J. Ionic liquids as amphiphile self-assembly media. *Chem. Soc. Rev.* **2008**, *37*, 1709–1726.
- (25) Hayes, R.; Imberti, S.; Warr, G. G.; Atkin, R. The Nature of Hydrogen Bonding in Protic Ionic Liquids. *Angew. Chem., Int. Ed. Engl.* **2013**, *52*, 4623–4627.

- (26) Shimizu, K.; Gomes, M. F. C.; Pádua, A. A.; Rebelo, L. P.; Lopes, J. N. C. Three commentaries on the nano-segregated structure of ionic liquids. *J. Mol. Struct.*: THEOCHEM **2010**, 946, 70–76.
- (27) National Academies of Sciences, Engineering, and Medicine A Research Agenda for Transforming Separation Science; The National Academies Press: Washington, DC, 2019; p 114. https://www.nap.edu/catalog/25421/a-research-agenda-for-transforming-separation-science.
- (28) Critical Minerals and Materials: U.S. Department of Energy's Strategy to Support Domestic Critical Mineral and Material Supply Chains, (FY 2021-F Y2031). https://www.energy.gov/sites/default/files/2007 1/01/f82/DOE%20Critical%20Minerals%20and%20Materials%20Strategy_0.pdf (accessed Nov, 15 2021).
- (29) U.S. DOE Basic Research Needs for Environmental Management: Report of the Office of Science Workshop on Environmental Management, U.S. Department of Energy Office of Science. 2016, https://science.osti.gov/-/media/bes/pdf/reports/2016/Basic_Research_Needs_for_Environmental_Management_rpt.pdf (accessed Oct. 25 2018).
- (30) Giwa, A.; Hasan, S. W.; Yousuf, A.; Chakraborty, S.; Johnson, D. J.; Hilal, N. Biomimetic membranes: A critical review of recent progress. *Desalination* **2017**, *420*, 403–424.
- (31) Sholl, D. S.; Lively, R. P. Seven chemical separations to change the world. *Nature* **2016**, 532, 435–437.
- (32) Radjenovic, J.; Sedlak, D. L. Challenges and Opportunities for Electrochemical Processes as Next-Generation Technologies for the Treatment of Contaminated Water. *Environ. Sci. Technol.* **2015**, 49, 11292–11302.
- (33) Su, X.; Tan, K.-J.; Elbert, J.; Rüttiger, C.; Gallei, M.; Jamison, T. F.; Hatton, T. A. Asymmetric Faradaic systems for selective electrochemical separations. *Energy Environ. Sci.* **2017**, *10*, 1272–1283
- (34) Su, X.; Kulik, H. J.; Jamison, T. F.; Hatton, T. A. Anion-Selective Redox Electrodes: Electrochemically Mediated Separation with Heterogeneous Organometallic Interfaces. *Adv. Funct. Mater.* **2016**, *26*, 3394—3404.
- (35) Ji, Y.; Goulet, M. A.; Pollack, D. A.; Kwabi, D. G.; Jin, S.; Porcellinis, D.; Kerr, E. F.; Gordon, R. G.; Aziz, M. J. A Phosphonate-Functionalized Quinone Redox Flow Battery at Near-Neutral pH with Record Capacity Retention Rate. *Adv. Energy Mater.* **2019**, *9*, 1900039.
- (36) Palakkal, V. M.; Valentino, L.; Lei, Q.; Kole, S.; Lin, Y. J.; Arges, C. G. Advancing electrodeionization with conductive ionomer binders that immobilize ion-exchange resin particles into porous wafer substrates. *npj Clean Water* **2020**, *3*, 5.
- (37) Park, S. J.; Joo, M. H.; Hong, S.-M.; Kang, J.-G.; Rhee, C. K.; Lee, S. W.; Sohn, Y. Electrochemical Eu (III) behaviours and Eu oxysulfate recovery over terpyridine-functionalized indium tin oxide electrodes. *Inorg. Chem. Front.* **2021**, *8*, 1175–1188.
- (38) Wadhawan, J. D.; Schröder, U.; Neudeck, A.; Wilkins, S. J.; Compton, R. G.; Marken, F.; Consorti, C. S.; de Souza, R. F.; Dupont, CI. r. Ionic liquid modified electrodes. Unusual partitioning and diffusion effects of Fe (CN) 64–/3– in droplet and thin layer deposits of 1-methyl-3-(2, 6-(S)-dimethylocten-2-yl)-imidazolium tetrafluoroborate. *J. Electroanal. Chem.* **2000**, 493, 75–83.
- (39) Fritz, P. A.; Boom, R. M.; Schroën, C. G. P. H. Electrochemically driven adsorptive separation techniques: From ions to proteins and cells in liquid streams. *Sep. Purif. Technol.* **2021**, *274*, 118754.
- (40) Li, Q.; Lu, D.; Zheng, J.; Jiao, S.; Luo, L.; Wang, C.-M.; Xu, K.; Zhang, J.-G.; Xu, W. Li+-Desolvation Dictating Lithium-Ion Battery's Low-Temperature Performances. *ACS Appl. Mater. Interfaces* **2017**, *9*, 42761–42768.
- (41) Chen, J. Application of Ionic Liquids on Rare Earth Green Separation and Utilization; Springer, 2015.
- (42) Fuerhacker, M.; Haile, T. M.; Kogelnig, D.; Stojanovic, A.; Keppler, B. Application of ionic liquids for the removal of heavy metals from wastewater and activated sludge. *Water Sci. Technol.* **2012**, *65*, 1765–1773.

- (43) Zhang, J.; Glezakou, V.-A.; Rousseau, R.; Nguyen, M.-T. NWPEsSe: An Adaptive-Learning Global Optimization Algorithm for Nanosized Cluster Systems. *J. Chem. Theory Comput.* **2020**, *16*, 3947.
- (44) Johnson, A. R.; Carlson, E. E. Collision-Induced Dissociation Mass Spectrometry: A Powerful Tool for Natural Product Structure Elucidation. *Anal. Chem.* **2015**, *87*, 10668–10678.
- (45) Gunaratne, K. D. D.; Prabhakaran, V.; Johnson, G. E.; Laskin, J. Gas-Phase Fragmentation Pathways of Mixed Addenda Keggin Anions: PMo12-nWnO403— (n=0-12). *J. Am. Soc. Mass Spectrom.* **2015**, 26, 1027—1035.
- (46) Yuan, Q.; Cao, W.; Wang, X.-B. Cryogenic and Temperature-Dependent Photoelectron Spectroscopy of Metal Complexes. *Int. Rev. Phys. Chem.* **2020**, 39, 83–108.
- (47) Johnson, G. E.; Lysonski, M.; Laskin, J. In situ reactivity and TOF-SIMS analysis of surfaces prepared by soft and reactive landing of mass-selected ions. *Anal. Chem.* **2010**, 82, 5718–5727.
- (48) Gunaratne, K. D. D.; Prabhakaran, V.; Ibrahim, Y. M.; Norheim, R. V.; Johnson, G. E.; Laskin, J. Design and performance of a high-flux electrospray ionization source for ion soft landing. *Analyst* **2015**, *140*, 2957–2963.
- (49) Kopanski, J. J.; Afridi, M. Y.; Jeliazkov, S.; Jiang, W.; Walker, T. R.; Seiler, D. G.; Diebold, A. C.; McDonald, R.; Garner, C. M.; Herr, D.; Khosla, R. P.; Secula, E. M. Scanning Kelvin Force Microscopy For Characterizing Nanostructures in Atmosphere. *AIP Conf. Proc.* **2007**, 931, 530–534.
- (50) Panchal, V.; Pearce, R.; Yakimova, R.; Tzalenchuk, A.; Kazakova, O. Standardization of surface potential measurements of graphene domains. *Sci. Rep.* **2013**, *3*, 2597.
- (51) Park Atomic Force Microscopy Application Note #61: A Comparative Study of Atomic Force Microscopy between AM KPFM and Sideband KPFM: Principles and Applications. https://parksystems.com/images/media/appnote/AppNote-61_sideband-KPFM_A-comparative-study.pdf (accessed Oct, 10 2021).
- (52) Zhang, J.; Dolg, M. ABCluster: the Artificial Bee Colony Algorithm for Cluster Global Optimization. *Phys. Chem. Chem. Phys.* **2015**, *17*, 24173–24181.
- (53) Zhang, J.; Dolg, M. Global Optimization of Clusters of Rigid Molecules Using the Artificial Bee Colony Algorithm. *Phys. Chem. Chem. Phys.* **2016**, *18*, 3003–3010.
- (54) Zhang, J.; Glezakou, V.-A. Global optimization of chemical cluster structures: Methods, applications, and challenges. *Int. J. Quantum Chem.* **2021**, *121* (7), e26553.
- (55) Bannwarth, C.; Ehlert, S.; Grimme, S. GFN2-xTB—An Accurate and Broadly Parametrized Self-Consistent Tight-Binding Quantum Chemical Method with Multipole Electrostatics and Density-Dependent Dispersion Contributions. *J. Chem. Theory Comput.* **2019**, *15*, 1652–1671.
- (56) Becke, A. D. Density-functional thermochemistry. III. The role of exact exchange. *J. Chem. Phys.* **1993**, *98*, 5648–5652.
- (57) Becke, A. D. Density-functional exchange-energy approximation with correct asymptotic behavior. *Phys. Rev. A* **1988**, *38*, 3098–3100.
- (58) Grimme, S.; Antony, J.; Ehrlich, S.; Krieg, H. A Consistent and Accurate Ab Initio Parametrization of Density Functional Dispersion Correction (DFT-D) for the 94 Elements H-Pu. *J. Chem. Phys.* **2010**, *132*, 154104.
- (59) Riplinger, C.; Neese, F. An efficient and near linear scaling pair natural orbital based local coupled cluster method. *J. Chem. Phys.* **2013**, *138*, 034106.
- (60) Berendsen, H. J. C.; Postma, J. P. M.; van Gunsteren, W. F.; DiNola, A.; Haak, J. R. Molecular dynamics with coupling to an external bath. *J. Chem. Phys.* **1984**, *81*, 3684–3690.
- (61) Lu, T.; Chen, F. Multiwfn: a multifunctional wavefunction analyzer. *J. Comput. Chem.* **2012**, 33, 580–592.
- (62) Neese, F. The ORCA program system. Wiley Interdiscip. Rev.: Comput. Mol. Sci. 2012, 2, 73–78.
- (63) Echt, O.; Sattler, K.; Recknagel, E. Magic Numbers for Sphere Packings: Experimental Verification in Free Xenon Clusters. *Phys. Rev. Lett.* **1981**, 47, 1121–1124.

- (64) Echt, O.; Reyes Flotte, A.; Knapp, M.; Sattler, K.; Recknagel, E. Magic Numbers in Mass Spectra of Xe, C2F4Cl2 and SF6 Clusters. *Ber. Bunsenges. Phys. Chem.* **1982**, *86*, 860–865.
- (65) Mühlbach, J.; Sattler, K.; Pfau, P.; Recknagel, E. Evidence for magic numbers of free lead-clusters. *Phys. Lett. A* **1982**, *87*, 415–417.
- (66) Zhang, D.; Cooks, R. G. Doubly charged cluster ions [(NaCl) m (Na) 2] 2+: magic numbers, dissociation, and structure. *Int. J. Mass Spectrom.* **2000**, 195–196, 667–684.
- (67) Gozzo, F. C.; Santos, L. S.; Augusti, R.; Consorti, C. S.; Dupont, J.; Eberlin, M. N. Gaseous Supramolecules of Imidazolium Ionic Liquids: "Magic" Numbers and Intrinsic Strengths of Hydrogen Bonds. *Chem.—Eur. J.* **2004**, *10*, 6187–6193.
- (68) Fernandes, A. M.; Coutinho, J. A. P.; Marrucho, I. M. Gas-phase dissociation of ionic liquid aggregates studied by electrospray ionisation mass spectrometry and energy-variable collision induced dissociation. *J. Mass Spectrom.* **2009**, *44*, 144–150.
- (69) Zhang, J.; Baxter, E. T.; Nguyen, M.-T.; Prabhakaran, V.; Rousseau, R.; Johnson, G. E.; Glezakou, V.-A. Structure and Stability of the Ionic Liquid Clusters [EMIM]n[BF4]n+1- (n = 1-9): Implications for Electrochemical Separations. *J. Phys. Chem. Lett.* **2020**, *11*, 6844–6851.
- (70) Dorbritz, S.; Ruth, W.; Kragl, U. Investigation on aggregate formation of ionic liquids. *Adv. Synth. Catal.* **2005**, 347, 1273–1279.
- (71) Chen, G.; Graham Cooks, R.; Bunk, D. M.; Welch, M. J.; Christie, J. R. Partitioning of kinetic energy to internal energy in the low energy collision-induced dissociations of proton-bound dimers of polypeptides. *Int. J. Mass Spectrom.* **1999**, *185–187*, 75–90.
- (72) Alexandrova, A. N.; Boldyrev, A. I.; Fu, Y.-J.; Yang, X.; Wang, X.-B.; Wang, L.-S. Structure of the NaxClx+1- (x=1-4) clusters via ab initio genetic algorithm and photoelectron spectroscopy. *J. Chem. Phys.* **2004**, *121*, 5709–5719.
- (73) Deng, S. H. M.; Kong, X.-Y.; Wang, X.-B. Probing the early stages of salt nucleation—Experimental and theoretical investigations of sodium/potassium thiocyanate cluster anions. *J. Chem. Phys.* **2015**, 142, 024313.
- (74) Riplinger, C.; Sandhoefer, B.; Hansen, A.; Neese, F. Natural triple excitations in local coupled cluster calculations with pair natural orbitals. *J. Chem. Phys.* **2013**, *139*, 134101.
- (75) Johnson, G. E.; Hu, Q.; Laskin, J. Soft landing of complex molecules on surfaces. *Annu. Rev. Anal. Chem* **2011**, *4*, 83–104.
- (76) Laskin, J.; Johnson, G. E.; Prabhakaran, V. Soft Landing of Complex Ions for Studies in Catalysis and Energy Storage. *J. Phys. Chem. C* **2016**, *120*, 23305–23322.
- (77) Laskin, J.; Johnson, G. E.; Warneke, J.; Prabhakaran, V. From Isolated Ions to Multilayer Functional Materials Using Ion Soft Landing. *Angew. Chem., Int. Ed. Engl.* **2018**, *57*, 16270–16284.
- (78) Cyriac, J.; Pradeep, T.; Kang, H.; Souda, R.; Cooks, R. G. Low-Energy Ionic Collisions at Molecular Solids. *Chem. Rev.* **2012**, *112*, 5356–5411.
- (79) Johnson, G. E.; Gunaratne, D.; Laskin, J. Soft- and reactive landing of ions onto surfaces: Concepts and applications. *Mass Spectrom. Rev.* **2016**, *35*, 439–479.
- (80) Sandford, C.; Edwards, M. A.; Klunder, K. J.; Hickey, D. P.; Li, M.; Barman, K.; Sigman, M. S.; White, H. S.; Minteer, S. D. A synthetic chemist's guide to electroanalytical tools for studying reaction mechanisms. *Chem. Sci.* **2019**, *10*, 6404–6422.
- (81) Prabhakaran, V.; Mehdi, B. L.; Ditto, J. J.; Engelhard, M. H.; Wang, B.; Gunaratne, K. D. D.; Johnson, D. C.; Browning, N. D.; Johnson, G. E.; Laskin, J. Rational design of efficient electrode–electrolyte interfaces for solid-state energy storage using ion soft landing. *Nat. Commun.* **2016**, *7*, 11399.
- (82) Daeneke, T.; Uemura, Y.; Duffy, N. W.; Mozer, A. J.; Koumura, N.; Bach, U.; Spiccia, L. Aqueous Dye-Sensitized Solar Cell Electrolytes Based on the Ferricyanide–Ferrocyanide Redox Couple. *Adv. Mater.* **2012**, *24*, 1222–1225.
- (83) Wijeratne, K.; Ail, U.; Brooke, R.; Vagin, M.; Liu, X.; Fahlman, M.; Crispin, X. Bulk electronic transport impacts on electron transfer at conducting polymer electrode—electrolyte interfaces. *Proc. Natl. Acad. Sci. U.S.A.* **2018**, *115*, 11899—11904.

Supporting Information

Functionalization of Electrodes with Tunable $[EMIM]_x[Cl]_{x+1}^-$ Ionic Liquid Clusters for Electrochemical Separations

Eric T. Baxter, Jun Zhang, Shuai Tan, Manh-Thuong Nguyen, Difan Zhang, Qinqin Yuan, Wenjin Cao, Xue-Bin Wang, Venkateshkumar Prabhakaran,* Vassiliki-Alexandra Glezakou,* and Grant E. Johnson*

Physical and Computational Sciences Directorate, Pacific Northwest National Laboratory,

Richland, Washington 99354, United States

*Email: venky@pnnl.gov, grant.johnson@pnnl.gov, vanda.glezakou@pnnl.gov

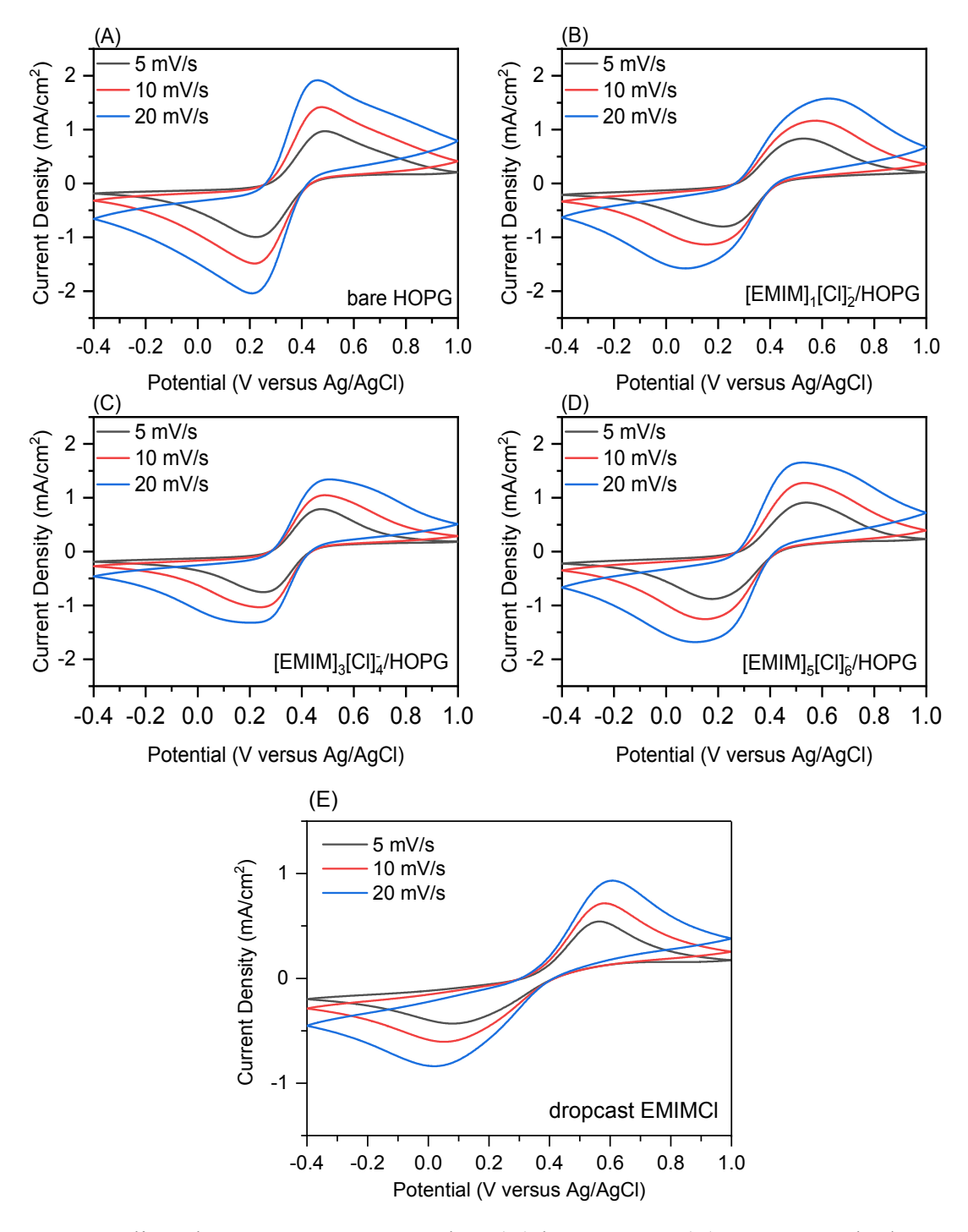


Figure S1. Cyclic voltammograms measured on (A) bare HOPG, (B) $[EMIM]_1[Cl]_2$ -/HOPG, (C) $[EMIM]_3[Cl]_4$ -/HOPG, and (D) $[EMIM]_5[Cl]_6$ -/HOPG with a Fe(CN)₆^{4-/3-} redox couple at different potential scan rates (5, 10, and 20 mV/s). The shape of the CV curves of EMIMCl clusters/HOPG

electrode did not significantly change during the different scan rate/cycles, which indicates that the EMIMCl clusters are quite stable on the HOPG electrode over 50 CV cycles.

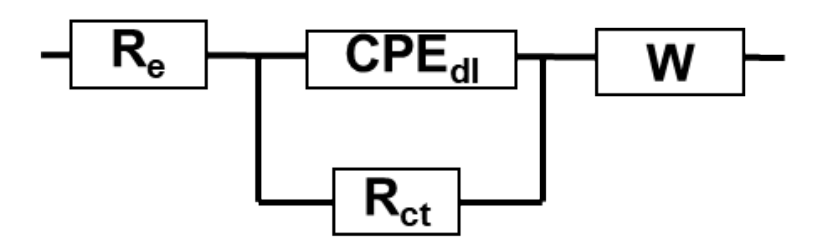


Figure S2. Equivalent circuit model used to fit the EIS data presented in Figure 10. $\mathbf{R_e}$ – Electrode resistance, ohms; $\mathbf{R_{ct}}$ – charge transfer resistance, ohms; $\mathbf{CPE_{dl}}$ – Constant phase element [non-homogenous capacitance given by $Z(\omega) = Q^{-1}(j^*\omega)^{-n}$]; **W** - Warburg diffusion (A_w : Warburg coefficient, Ohm s^{-0.5}).

Table 1. Calculated frequencies for $[(EMIM)_x(Cl)_{x+1}]^-$

1 (anion)	2 (anion)	3 (anion)	4 (anion)	5 (anion)	6 (anion)
28.96	42.12	30.99	24.75	22.73	18.08
68.61	50.10	35.61	26.72	27.98	27.59
74.67	55.53	37.91	30.80	30.01	29.13
113.02	65.78	44.22	35.19	32.82	30.35
129.01	71.18	50.40	36.90	37.20	34.17
142.26	85.42	51.06	47.81	38.69	35.83
165.90	87.16	61.48	51.55	41.56	37.08
186.46	94.20	63.92	55.56	45.18	38.85
197.50	99.14	68.53	57.16	46.60	40.39
239.00	102.36	72.96	60.51	48.21	43.40
242.43	111.34	75.13	65.14	49.76	46.02
325.83	122.60	81.87	68.70	52.59	48.23
403.11	125.22	83.08	70.18	54.33	49.53
451.43	130.72	87.17	73.09	60.05	53.86
615.67	149.18	96.26	73.94	62.11	54.36
646.65	158.12	102.87	81.15	64.70	55.21
685.95	164.50	110.87	84.77	67.67	57.74
725.63	196.03	115.76	87.81	71.43	58.07
756.33	198.75	126.87	94.35	75.12	61.86
811.61	209.27	133.57	95.83	78.66	63.54
967.98	216.14	136.28	104.33	80.04	65.74
970.81	232.29	143.68	110.08	84.43	68.94
1009.31	258.27	145.30	113.05	86.39	71.71
1041.60	261.81	150.29	114.99	89.45	73.58
1066.67	288.17	152.27	118.35	90.46	75.76
1112.09	314.52	165.19	122.14	92.26	77.47
1115.78	329.45	175.62	130.15	94.48	79.34
1122.66	402.66	188.41	131.59	99.85	81.31
1131.28	407.88	204.38	134.15	101.42	84.90
1158.84	451.59	208.49	140.54	107.52	88.83
1202.48	455.04	213.17	143.67	111.12	90.99
1265.05	611.17	214.87	148.08	115.40	92.58
1314.36	617.69	216.35	150.86	117.97	93.91
1359.70	628.44	245.64	155.84	124.30	97.79
1383.29	643.98	251.51	160.03	127.85	101.55
1401.99	658.63	262.26	169.37	130.30	105.65
1407.58	674.44	264.39	172.98	132.08	107.33
1440.03	727.75	264.60	180.09	136.96	110.81
1446.04	730.50	286.45	183.74	139.37	112.30

1451.37	753.10	323.07	194.02	146.67	116.62
1463.88	792.56	325.71	198.55	152.21	119.12
1477.84	814.44	328.40	198.85	157.35	121.60
1479.34	843.26	376.78	206.22	160.36	125.63
1504.86	845.88	393.41	208.88	167.77	128.78
1605.18	862.48	396.15	217.50	173.90	132.74
1622.52	914.68	455.79	221.55	179.31	134.18
2787.87	948.62	458.78	244.66	182.28	138.73
2892.01	981.32	465.53	250.87	187.90	141.67
2921.63	986.57	609.45	260.04	189.64	146.48
3027.56	1059.48	613.81	264.09	194.57	149.97
3039.20	1064.07	614.05	269.98	202.91	153.40
3091.34	1073.84	635.85	307.67	205.97	154.80
3129.42	1079.59	641.55	319.28	214.60	160.22
3136.36	1112.51	643.64	320.90	216.25	166.43
3139.60	1115.16	669.38	326.00	218.08	167.58
3147.23	1118.82	679.01	332.38	236.44	171.38
3285.02	1124.42	681.14	389.18	238.51	175.27
3203.02	1136.64	725.05	398.57	241.51	178.20
	1140.31	730.10	403.39	246.51	182.51
	1147.66	735.45	412.64	257.23	184.34
	1153.78	741.79	444.12	258.84	190.66
	1156.22	752.10	447.48	260.56	202.63
	1161.62	786.31	456.38	264.60	211.74
	1209.78	802.17	458.03	267.81	219.27
	1213.98	816.58	607.81	272.12	220.26
	1281.76	836.46	610.84	280.05	228.48
	1285.78	860.47	611.84	315.02	234.32
	1324.16	864.11	616.09	322.22	234.74
	1328.59	890.53	629.13	325.64	237.56
	1371.97	896.93	642.42	329.23	240.40
	1378.65	921.05	645.71	331.25	244.01
	1393.57	983.13	651.34	386.11	245.86
	1395.80	984.24	668.23	390.80	246.69
	1408.57	984.48	676.39	398.44	251.58
	1417.76	1010.37	682.23	399.08	257.37
	1423.07	1056.18	685.66	401.31	258.42
	1426.16	1065.48	727.93	444.46	260.56
	1426.16	1003.48	727.93	448.41	262.06
	1443.34	1077.56	728.02	450.67	269.21
	1445.34	1077.30	731.10	450.07	271.41
	1440.87	1080.10	746.74	452.34	309.89
	1439.11	1081.36	762.06	607.01	312.39
	1463.16	1112.85	782.00	610.43	312.39
	1469.72	1114.65	783.95	611.61	316.15
	1474.25	1116.04	819.92	614.94	323.98

			1	
1477.5	7 1126.03	828.86	617.91	326.31
1481.89	9 1126.73	830.99	640.47	362.99
1489.54	1127.55	839.10	645.51	387.16
1499.63	3 1137.51	845.76	646.23	402.56
1503.80	5 1139.06	851.59	648.40	403.10
1506.00	1144.75	867.38	663.90	408.89
1613.83	3 1151.40	914.45	670.04	410.82
1615.9:	5 1153.40	938.21	671.39	436.93
1623.4	1154.53	941.21	683.64	438.91
1626.50	5 1162.30	969.28	687.93	446.14
2980.23	3 1165.93	974.92	688.86	448.93
3007.54	1210.99	982.39	724.05	450.82
3025.0	l l	983.17	726.85	468.18
3034.7	1 1220.07	983.85	727.04	613.18
3041.20		984.93	730.23	613.89
3045.1:		1051.00	730.54	615.00
3092.82		1059.68	753.05	616.00
3100.2		1066.27	767.00	618.54
3113.34		1068.74	788.10	623.88
3115.93		1070.88	790.70	642.70
3122.00		1075.17	801.30	643.96
3132.34		1078.31	809.93	645.51
3134.92		1084.86	813.60	648.61
3137.0		1108.70	817.85	651.69
3138.09		1109.42	820.57	652.46
3139.90		1110.54	824.18	672.97
3160.50		1113.24	846.90	675.18
3170.73		1114.71	851.04	678.42
3171.02		1115.04	886.23	679.41
3176.24		1116.38	903.75	681.89
3188.89		1123.74	904.95	683.89
3195.63		1130.41	908.23	724.74
3173.0.	1431.21	1130.41	910.32	725.48
	1441.04	1142.07	937.21	726.31
	1442.87	1142.82	955.15	728.09
	1452.21	1142.62	972.19	728.18
	1455.09	1147.03	980.59	733.19
	1460.47	1149.39	982.86	770.07
	1460.96	1154.06	984.00	773.85
	1466.05	1155.13	989.16	776.97
	1468.03	1155.74	989.85	791.28
	1468.93	1157.01	1057.92	796.39
	1471.45	1166.79	1061.12	812.02
	1472.64	1205.06	1062.68	813.55
	1474.55	1206.38	1063.46	814.62
	1480.15	1209.44	1066.57	817.39

1	1.401.00	1222.07	1070.04	020.61
	1481.92	1222.96	1070.84	820.61
	1488.89	1275.11	1073.61	821.19
	1489.57	1279.20	1075.76	836.31
	1498.87	1286.72	1077.16	843.96
	1500.32	1287.22	1079.90	846.31
	1501.72	1323.32	1106.73	878.13
	1514.60	1324.54	1107.40	880.16
	1615.86	1326.46	1109.87	887.12
	1618.62	1328.74	1113.34	901.35
	1621.71	1373.05	1116.57	902.73
	1623.67	1378.78	1117.83	921.54
	1626.78	1382.38	1119.92	931.98
	1635.57	1383.40	1122.43	941.86
	2902.59	1388.56	1123.27	943.05
	2994.64	1390.23	1123.95	979.77
	3004.98	1396.61	1126.06	980.07
	3011.76	1405.05	1126.98	983.61
	3017.46	1408.51	1127.89	983.77
	3026.48	1414.15	1136.21	986.04
	3033.63	1417.50	1136.70	987.61
	3043.53	1419.13	1139.11	988.98
	3044.08	1422.62	1140.42	1057.47
	3062.91	1426.17	1143.61	1060.38
	3081.92	1427.08	1144.28	1062.46
	3094.80	1428.42	1145.82	1065.24
	3113.57	1433.18	1155.14	1066.65
	3120.18	1440.10	1161.86	1068.88
	3125.85	1441.42	1163.22	1069.49
	3127.03	1452.27	1164.47	1071.11
	3128.22	1456.12	1190.61	1073.34
	3132.25	1460.42	1198.82	1074.02
	3134.98	1461.61	1201.35	1079.56
	3136.84	1462.38	1205.06	1080.03
	3142.20	1462.54	1212.76	1098.38
	3143.32	1464.47	1221.11	1107.22
	3146.28	1465.53	1271.62	1107.42
	3153.53	1468.16	1273.33	1112.62
	3156.23	1469.51	1273.49	1112.93
	3164.48	1470.07	1275.68	1113.72
	3167.30	1471.30	1281.44	1115.04
	3171.87	1473.76	1318.45	1116.56
	3175.09	1476.12	1319.46	1119.99
	3233.85	1477.60	1320.98	1122.73
	3249.96	1483.80	1323.61	1125.04
	3286.28	1486.43	1329.66	1126.73
	3338.36	1486.62	1364.10	1128.24
	5550.50	1 100.02	1501.10	1120,21

1488.59	1374.77	1128.77
1490.53	1376.28	1129.41
1499.83	1378.58	1135.24
1500.24	1380.48	1136.00
1505.05	1385.34	1138.83
1510.54	1389.90	1139.78
1519.66	1390.71	1147.58
1617.58	1390.93	1148.69
1619.24	1395.26	1150.72
1621.16	1401.29	1151.86
1624.08	1413.17	1152.69
1624.74	1416.50	1154.42
1627.22	1418.49	1160.16
1627.93	1419.21	1161.52
1636.10	1419.94	1163.35
2891.46	1421.94	1164.48
2980.62	1423.88	1166.30
3006.10	1428.85	1202.04
3013.68	1430.91	1206.80
3019.85	1430.91	1208.96
3021.05	1438.23	1208.90
3022.80	1441.95	1215.37
3038.27	1443.83	1226.20
3040.15	1450.85	1265.09
3043.43	1454.68	1273.54
3045.84	1456.14	1277.24
3046.30	1460.06	1277.77
3064.73	1461.07	1282.94
3081.35	1461.81	1285.27
3094.78	1462.31	1316.84
3105.76	1462.94	1318.39
3115.15	1464.84	1320.50
3118.77	1466.76	1324.11
3123.43	1467.91	1328.94
3126.81	1468.75	1334.80
3127.01	1469.66	1360.38
3127.23	1470.92	1361.62
3133.34	1472.23	1366.70
3138.18	1472.61	1377.99
3139.87	1477.67	1380.40
3140.84	1478.45	1381.89
3142.79	1481.46	1385.70
3142.95	1484.32	1389.50
3145.46	1484.80	1389.73
3146.91	1486.15	1390.79
3147.90	1489.71	1391.42
5117.50	1 107./1	10/1.12

3148.64	1490.97	1391.68
3149.66	1491.41	1392.32
3155.17	1496.41	1395.24
3166.15	1498.06	1411.59
3173.20	1499.82	1414.40
3176.34	1503.30	1415.43
3190.74	1504.87	1416.11
3197.08	1510.26	1423.03
3219.11	1614.21	1424.19
3264.28	1614.35	1424.88
3279.47	1614.59	1426.54
3282.49	1618.25	1427.54
3363.81	1620.59	1430.33
3303.81	1622.42	1434.75
	1622.42	1434.73
	1626.19	1440.10
	1627.34	1440.55
	1628.36	1443.18
	3002.22	1443.58
	3003.77	1451.57
	3009.79	1455.21
	3012.20	1457.33
	3013.17	1459.05
	3017.22	1461.57
	3031.44	1462.00
	3034.96	1463.81
	3039.05	1465.05
	3040.96	1466.20
	3047.11	1467.12
	3047.39	1467.88
	3057.96	1468.07
	3068.01	1468.74
	3069.44	1470.76
	3077.51	1471.00
	3082.44	1471.26
	3093.49	1472.40
	3105.89	1472.65
	3112.41	1473.26
	3114.48	1476.08
	3120.98	1477.40
	3121.22	1477.45
	3124.08	1477.88
	3124.70	1479.35
	3125.63	1482.52
	3128.48	1485.13
	3129.69	1489.36
	5147.07	1707.30

		3132.29	1491.94
		3137.83	1496.96
		3138.01	1498.55
		3138.17	1501.31
		3140.02	1501.93
		3142.11	1502.77
		3143.49	1503.44
		3144.11	1505.38
		3145.51	1507.96
		3148.08	1616.03
		3148.91	1618.05
		3153.02	1618.70
		3153.46	1620.67
		3155.58	1621.28
		3161.43	1622.49
		3169.21	
			1624.31
		3172.87	1625.31
		3177.25	1625.84
		3181.29	1627.21
		3191.81	1628.21
		3217.31	1631.35
		3223.91	2993.87
		3226.58	3016.11
		3243.78	3018.06
		3245.03	3018.90
		3271.73	3023.15
		3310.08	3026.66
			3028.77
			3031.59
			3039.80
			3040.23
			3040.70
			3046.99
			3047.16
			3048.06
			3048.42
			3053.86
			3065.75
			3068.25
			3070.18
			3093.90
			3106.07
			3115.35
			3115.88
			3118.49
			3121.58
			J141.JU

	T	Г	Г	T	T
					3127.31
					3128.46
					3133.52
					3133.71
					3135.00
					3135.78
					3136.13
					3137.65
					3138.26
					3140.29
					3141.92
					3142.84
					3143.18
					3143.68
					3145.25
					3147.18
					3148.68
					3149.29
					3152.60
					3153.93
					3154.48
					3156.29
					3158.15
					3159.20
					3159.48
					3162.80
					3165.91
					3168.76
					3170.76
					3171.07
					3174.56
					3177.72
					3186.34
					3192.83
					3197.29
					3201.60
					3215.91
					3237.85
					3239.33
					3261.72
					3295.26
1 (neutral)	2 (neutral)	3 (neutral)	4 (neutral)	5 (neutral)	6 (neutral)
19.67	30.95	25.95	17.98	19.72	11.09
56.16	40.59	35.31	24.69	20.51	17.82
59.24	44.21	41.12	29.46	28.41	19.27
86.29	47.74	47.39	31.83	29.34	27.80

107.91	61.79	49.96	33.89	33.13	30.86
124.29	70.10	53.55	39.00	35.71	31.72
133.95	76.78	56.86	40.73	38.32	37.38
146.85	89.14	57.77	46.56	42.35	39.34
159.31	96.03	63.86	47.65	46.22	40.74
217.52	100.32	68.03	49.68	47.74	41.87
243.66	103.74	70.33	53.24	49.30	45.29
314.10	107.01	75.87	54.12	50.18	48.14
395.78	116.09	78.61	57.71	52.99	51.01
441.79	121.69	83.93	64.00	55.90	53.27
612.03	128.17	87.83	65.34	56.09	53.94
646.70	143.45	98.62	69.24	61.14	55.68
681.85	153.05	102.19	76.05	62.01	58.28
721.84	164.73	111.39	76.99	65.79	60.04
771.51	168.42	121.69	79.05	70.53	61.37
796.71	192.41	126.44	83.04	73.52	64.04
920.35	211.76	131.21	93.79	76.10	65.21
935.37	220.66	137.70	100.46	79.35	70.13
975.80	226.05	141.96	104.14	81.88	71.23
1055.58	251.58	146.45	108.10	83.05	72.80
1063.25	268.72	149.90	110.98	87.83	75.10
1105.28	306.23	163.07	114.19	91.24	78.46
1111.96	322.58	164.97	120.21	92.69	81.16
1119.74	403.91	184.32	122.58	96.57	82.00
1128.50	408.52	189.14	128.60	99.73	87.99
1151.40	437.01	200.76	131.40	103.20	88.31
1196.28	441.05	202.99	132.22	106.41	89.42
1265.32	610.62	212.79	143.98	108.86	94.36
1312.93	610.91	215.31	146.11	112.17	95.32
1365.83	640.38	238.53	150.55	117.44	98.51
1383.21	642.41	240.14	157.03	121.17	101.96
1402.91	662.69	254.45	160.27	121.56	103.51
1422.07	670.69	256.36	168.67	123.93	104.54
1442.49	716.81	257.32	170.29	128.38	108.26
1453.62	726.14	278.45	175.29	134.86	110.94
1459.53	727.05	317.93	179.80	139.70	112.81
1464.22	748.93	318.24	186.40	142.07	115.43
1469.39	797.20	322.89	191.73	147.49	120.39
1473.82	825.17	390.11	192.86	152.93	121.74
1501.02	831.67	396.03	212.03	157.40	125.67
1622.34	845.62	398.40	213.92	163.19	129.64
1624.70	875.60	446.35	215.32	166.68	130.79
3047.14	905.98	450.35	227.16	168.62	135.62
3053.15	979.64	454.54	249.42	178.24	139.42
3067.76	980.58	575.02	258.24	182.82	140.98
3090.56	1059.96	610.56	259.52	190.12	145.97
3070.30	1037.70	010.50	237.32	170.12	173.71

3149.57	1061.11	612.28	273.66	196.09	150.47
3160.04	1071.76	616.10	306.67	211.61	152.17
3160.04	1071.76	639.39	316.54	212.85	157.36
3168.72	1104.85	640.58			
			319.79	213.71 215.02	162.90
3169.36	1106.03	649.83	320.69		164.17
3187.46	1112.08	666.76	322.77	218.50	166.80
3294.68	1118.32	673.26	396.26	227.99	169.52
	1124.07	724.40	396.68	240.11	171.00
	1126.66	726.17	399.25	245.10	173.72
	1134.78	734.33	403.11	251.79	184.75
	1145.99	736.63	441.92	253.05	187.91
	1150.39	744.05	445.04	258.86	189.82
	1150.42	766.93	446.94	261.52	190.27
	1191.67	804.35	448.61	263.36	200.46
	1198.71	807.65	608.21	282.54	205.82
	1268.68	817.33	610.41	305.92	210.55
	1273.26	829.66	612.13	313.64	210.94
	1314.05	838.52	615.06	320.48	213.99
	1316.58	854.12	624.59	320.97	214.82
	1367.88	895.56	638.97	321.78	219.85
	1383.21	972.44	642.49	381.48	234.81
	1391.90	974.13	643.95	385.79	244.25
	1394.31	977.77	657.56	392.59	251.58
	1403.21	981.20	664.36	395.60	255.69
	1407.75	1041.51	677.35	401.30	257.80
	1410.76	1049.03	679.80	440.56	259.74
	1426.44	1058.40	720.82	445.29	263.72
	1427.01	1060.34	724.81	446.67	264.78
	1438.75	1072.00	725.65	447.20	267.86
	1446.24	1074.81	731.46	448.10	289.41
	1451.15	1080.09	732.44	606.91	304.96
	1459.55	1104.65	734.41	608.57	316.01
	1460.45	1105.59	758.62	609.47	322.44
	1463.77	1106.87	764.45	612.30	326.58
	1467.03	1110.85	783.77	613.84	328.76
	1474.39	1117.62	794.31	636.95	331.61
	1476.46	1120.44	814.25	641.94	366.27
	1481.00	1127.32	815.94	645.69	381.64
	1486.57	1135.11	819.97	647.57	400.85
	1492.57	1136.04	821.47	655.52	402.68
	1501.60	1141.26	848.19	663.63	402.08
	1589.53	1141.20	876.76	667.02	404.48
	1609.01	1147.39	909.89	679.67	443.32
	1615.86	1153.75	913.38	684.63	445.04
	1630.14	1158.15	945.50	685.60	447.60
	3036.19	1161.48	959.45	722.65	448.62

3043.09	1200.14	976.52	724.32	453.36
3043.09		970.32	725.25	
	1206.53			463.20
3052.18	1210.75	980.66	727.83	601.61
3057.76	1266.33	981.33	728.66	607.24
3085.02	1272.02	1052.45	736.95	610.15
3127.06	1277.42	1060.27	769.24	613.11
3140.99	1315.44	1061.13	774.32	614.79
3150.74	1320.46	1061.59	775.97	616.64
3153.53	1329.11	1068.87	798.35	623.27
3153.82	1350.41	1069.83	799.90	640.82
3154.27	1378.16	1075.36	801.35	643.59
3155.21	1380.97	1077.48	811.11	646.08
3163.40	1385.55	1103.95	813.27	651.07
3169.42	1389.34	1107.10	816.45	652.03
3171.35	1392.37	1107.41	818.62	659.45
3181.74	1401.60	1107.62	830.66	673.22
3190.27	1405.98	1110.41	870.04	673.82
3200.72	1413.79	1111.36	873.38	681.72
3260.83	1415.94	1113.46	887.99	683.32
3287.20	1426.96	1115.37	898.50	684.53
3313.09	1427.71	1125.28	903.50	726.18
	1429.27	1127.29	930.17	726.78
	1439.63	1128.51	940.38	728.54
	1440.03	1136.00	949.69	729.29
	1440.68	1138.92	980.09	731.57
	1461.59	1142.06	980.39	732.28
	1461.73	1143.71	980.95	757.18
	1466.64	1145.12	985.42	758.44
	1467.28	1150.36	986.88	764.36
	1468.99	1150.79	1055.61	776.55
	1469.14	1150.81	1060.04	790.30
	1471.32	1153.98	1062.90	794.17
	1472.87	1199.73	1063.15	812.93
	1474.55	1202.33	1065.57	815.07
	1475.37	1203.18	1069.35	819.65
	1488.03	1207.91	1070.00	826.55
	1489.29	1266.04	1070.53	829.05
	1492.55	1268.57	1072.55	830.76
	1492.33	1274.42	1073.03	833.37
	1493.09	1278.74	1104.70	834.58
	1503.19	1314.24	1104.70	840.62
	1504.04	1315.56	1107.12	881.95
	1563.02	1316.20	1107.87	888.85
	1592.76	1318.02	1113.28	891.31
	1617.78	1373.38	1114.12	903.68
	1620.39	1377.70	1114.68	907.45

1.00.00	1270 14	1116.00	020.05
1626.23	1379.14	1116.89	938.95
1631.55	1379.55	1117.81	955.48
2928.84	1387.82	1119.92	972.63
3015.33	1392.55	1122.85	976.45
3017.45	1394.47	1123.64	978.43
3024.73	1396.50	1124.88	979.70
3041.84	1402.15	1127.86	984.19
3043.84	1407.77	1132.86	987.83
3050.86	1408.92	1133.56	993.80
3053.83	1409.30	1133.83	1010.74
3054.52	1415.87	1136.92	1046.39
3071.15	1422.08	1140.85	1057.40
3093.59	1425.92	1142.12	1057.87
3126.94	1426.40	1146.38	1061.11
3134.69	1428.28	1157.43	1061.55
3137.57	1433.97	1157.51	1062.26
3139.12	1435.68	1160.28	1065.32
3142.25	1437.01	1175.25	1071.61
3150.64	1438.10	1190.43	1071.91
3151.55	1454.46	1193.91	1076.69
3155.94	1457.88	1198.43	1078.73
3156.25	1459.91	1210.00	1079.54
3158.78	1460.18	1212.11	1092.51
3160.70	1461.49	1268.24	1099.09
3167.54	1461.70	1268.84	1105.92
3170.47	1462.27	1270.33	1107.19
3170.90	1464.55	1270.65	1108.15
3174.44	1466.87	1273.74	1108.95
3187.88	1468.74	1309.05	1110.66
3203.18	1469.00	1316.09	1111.86
3208.97	1470.43	1317.57	1112.54
3275.46	1471.86	1318.20	1114.53
3293.16	1472.59	1323.13	1114.89
3310.41	1477.67	1363.65	1116.38
3382.31	1481.95	1370.11	1117.89
3302.31	1483.16	1379.43	1127.30
	1484.52	1382.17	1127.50
	1496.28	1382.17	1133.61
	1490.28	1384.26	1134.43
	1501.89	1384.26	1134.43
	1502.48	1389.17	1136.21
	1504.69	1389.17	1136.21
	1575.79 1603.81	1393.70 1401.16	1143.80 1146.24
	1615.81	1408.83	1149.44
	1621.65	1410.96	1150.11

	1623.85	1411.76	1151.06
	1625.48	1412.73	1152.23
	1631.06	1414.82	1153.45
	1632.83	1415.72	1154.45
	3022.15	1422.76	1157.25
	3038.15	1423.15	1172.89
	3042.52	1430.66	1184.84
	3043.39	1432.40	1189.96
	3049.70	1434.72	1192.69
	3050.15	1435.26	1211.86
	3050.62	1442.37	1213.91
	3052.15	1443.24	1230.61
	3054.93	1447.38	1269.99
	3057.54	1448.02	1271.10
	3063.60	1453.23	1273.54
	3065.39	1459.72	1275.13
	3103.49	1459.98	1281.41
	3117.85	1461.39	1287.69
	3121.10	1461.99	1310.45
	3123.76	1462.44	1314.06
	3126.49	1462.83	1319.89
	3129.99	1463.40	1321.80
	3138.06	1465.95	1324.18
	3138.27	1466.30	1325.74
	3144.44	1467.17	1352.81
	3148.62	1468.89	1365.41
	3151.17	1469.17	1367.27
	3151.55	1470.87	1374.18
	3152.07	1472.48	1376.69
	3153.54	1477.16	1381.44
	3154.62	1477.54	1381.68
1	3156.65	1480.29	1383.33
	3159.57	1482.19	1385.93
	3160.26	1482.77	1391.37
	3161.55	1484.34	1392.39
	3165.05	1485.46	1394.09
	3167.79	1489.38	1394.75
	3183.36	1491.83	1395.97
1	3184.75	1493.00	1405.41
	3187.02	1494.52	1408.99
	3190.87	1498.82	1409.93
	3221.95	1507.42	1412.67
1	3243.50	1603.52	1414.77
	3284.20	1614.31	1417.06
	3295.34	1615.17	1419.00
	3297.76	1615.44	1425.63
	5471.10	1013.77	1743.03

	1.610.00	1.10 6.70
3305.04	1618.92	1426.78
3320.30	1619.59	1427.83
	1622.46	1430.40
	1624.17	1435.43
	1626.31	1436.86
	1627.83	1439.25
	2965.89	1441.65
	3019.18	1442.92
	3026.89	1449.25
	3028.87	1452.56
	3030.54	1456.18
	3036.51	1459.06
	3040.99	1459.49
	3042.56	1460.26
	3049.65	1460.89
	3051.11	1461.98
	3052.01	1462.68
	3055.47	1463.65
	3059.59	1464.56
	3062.64	1465.24
	3070.36	1468.14
	3081.68	1469.50
	3082.00	1469.78
	3098.76	1472.34
	3114.23	1472.60
	3114.23	1472.79
	3120.52	1472.79
	3126.00	1473.90
	3132.60	1476.93
	3132.60	1476.93
	3139.30	
		1478.40
	3142.20	1478.96
	3143.60	1480.30
	3146.16	1481.44
	3147.66	1487.74
	3150.06	1489.30
	3150.78	1489.90
	3153.90	1497.29
	3155.08	1498.04
	3156.15	1499.02
	3157.56	1501.06
	3157.92	1503.60
	3158.92	1505.21
	3159.37	1506.52
	3159.66	1554.64
	3166.87	1582.51

		3167.43	1614.81
		3169.09	1616.28
		3179.69	1617.86
		3181.02	1620.95
		3184.98	1622.95
		3191.06	1625.66
		3235.48	1626.41
		3240.24	1628.74
		3243.51	1630.75
		3255.28	1638.00
		3265.09	2944.85
		3272.76	2996.06
		3275.49	3008.34
		3280.19	3010.07
		3310.27	3021.78
		3310.27	
			3023.81
			3036.84
			3037.49
			3043.48
			3045.68
			3046.11
			3049.17
			3052.77
			3054.15
			3054.30
			3055.36
			3056.22
			3057.46
			3062.51
			3063.38
			3078.39
			3097.20
			3102.81
			3116.52
			3121.51
			3122.17
			3125.58
			3126.58
			3127.50
			3128.49
			3130.66
			3132.80
			3136.71
			3143.63
			3147.23
			3148.26
1	I		J110.20

3148.64 3151.85 3152.83 3154.03 3155.18 3155.64 3158.20 3159.91 3168.99 3170.82 3172.87 3179.76 3182.06 3184.76 3185.85 3188.31 3188.62 3200.51 3201.06 3206.16 3215.21 3219.80 3236.29 3243.82 3269.68 3228.76 3297.53 3306.27 3312.22 3321.84	1		
3152.83 3154.03 3155.18 3155.64 3158.20 3159.91 3168.99 3170.82 3172.87 3179.76 3182.06 3184.76 3188.31 3188.62 3200.51 3201.06 3206.16 3215.21 3219.80 3236.29 3243.82 3269.68 3288.76 3297.53 3306.27 3312.22			
3154.03 3155.18 3155.64 3158.20 3159.91 3168.99 3170.82 3172.87 3179.76 3182.06 3184.76 3185.85 3188.31 3188.62 3200.51 3201.06 3206.16 3215.21 3219.80 3236.29 3243.82 3269.68 3288.76 3297.53 3306.27 3312.22			
3155.18 3155.64 3158.20 3159.91 3168.99 3170.82 3172.87 3179.76 3182.06 3184.76 3185.85 3188.31 3188.62 3200.51 3201.06 3206.16 3215.21 3219.80 3236.29 3243.82 3269.68 3288.76 3297.53 3306.27 3312.22			3152.83
3155.64 3158.20 3159.91 3168.99 3170.82 3172.87 3179.76 3182.06 3184.76 3185.85 3188.31 3188.62 3200.51 3201.06 3206.16 3215.21 3219.80 3236.29 3243.82 3269.68 3288.76 3297.53 3306.27 3312.22			3154.03
3158.20 3159.91 3168.99 3170.82 3172.87 3179.76 3182.06 3184.76 3185.85 3188.31 3188.62 3200.51 3201.06 3206.16 3215.21 3219.80 3236.29 3243.82 3269.68 3288.76 3297.53 3306.27 3312.22			3155.18
3159.91 3168.99 3170.82 3172.87 3179.76 3182.06 3184.76 3185.85 3188.31 3188.62 3200.51 3201.06 3206.16 3215.21 3219.80 3236.29 3243.82 3269.68 3287.6 3297.53 3306.27 3312.22			3155.64
3168.99 3170.82 3172.87 3179.76 3182.06 3184.76 3185.85 3188.31 3188.62 3200.51 3201.06 3206.16 3215.21 3219.80 3236.29 3243.82 3269.68 3288.76 3297.53 3306.27 3312.22			3158.20
3170.82 3172.87 3179.76 3182.06 3184.76 3185.85 3188.31 3188.62 3200.51 3201.06 3206.16 3215.21 3219.80 3236.29 3243.82 3269.68 3288.76 3297.53 3306.27 3312.22			3159.91
3172.87 3179.76 3182.06 3184.76 3185.85 3188.31 3188.62 3200.51 3201.06 3206.16 3215.21 3219.80 3236.29 3243.82 3269.68 3288.76 3297.53 3306.27 3312.22			3168.99
3179.76 3182.06 3184.76 3185.85 3188.31 3188.62 3200.51 3201.06 3206.16 3215.21 3219.80 3236.29 3243.82 3269.68 3288.76 3297.53 3306.27 3312.22			3170.82
3182.06 3184.76 3185.85 3188.31 3188.62 3200.51 3201.06 3206.16 3215.21 3219.80 3236.29 3243.82 3269.68 3288.76 3297.53 3306.27 3312.22			3172.87
3184.76 3185.85 3188.31 3188.62 3200.51 3201.06 3206.16 3215.21 3219.80 3236.29 3243.82 3269.68 3288.76 3297.53 3306.27 3312.22			3179.76
3185.85 3188.31 3188.62 3200.51 3201.06 3206.16 3215.21 3219.80 3236.29 3243.82 3269.68 3288.76 3297.53 3306.27 3312.22			3182.06
3188.31 3188.62 3200.51 3201.06 3206.16 3215.21 3219.80 3236.29 3243.82 3269.68 3288.76 3297.53 3306.27 3312.22			3184.76
3188.62 3200.51 3201.06 3206.16 3215.21 3219.80 3236.29 3243.82 3269.68 3288.76 3297.53 3306.27 3312.22			3185.85
3200.51 3201.06 3206.16 3215.21 3219.80 3236.29 3243.82 3269.68 3288.76 3297.53 3306.27 3312.22			3188.31
3201.06 3206.16 3215.21 3219.80 3236.29 3243.82 3269.68 3288.76 3297.53 3306.27 3312.22			3188.62
3206.16 3215.21 3219.80 3236.29 3243.82 3269.68 3288.76 3297.53 3306.27 3312.22			3200.51
3215.21 3219.80 3236.29 3243.82 3269.68 3288.76 3297.53 3306.27 3312.22			3201.06
3219.80 3236.29 3243.82 3269.68 3288.76 3297.53 3306.27 3312.22			3206.16
3236.29 3243.82 3269.68 3288.76 3297.53 3306.27 3312.22			3215.21
3243.82 3269.68 3288.76 3297.53 3306.27 3312.22			
3269.68 3288.76 3297.53 3306.27 3312.22			
3288.76 3297.53 3306.27 3312.22			3243.82
3297.53 3306.27 3312.22			
3306.27 3312.22			
3312.22			3297.53
			3306.27
3321.84			
			3321.84